



Hybrid biomaterial hydrogel loading iRGD&PS double modified lipid nanoparticles ameliorates diabetic wound healing through promoting efferocytosis and glycolysis-related macrophage reprogramming

Wenqian Zhang^{a,b}, Shengming Zhang^{a,b}, Samuel Knoedler^c, Wenhao Han^d, Kangkang Zha^{a,b}, Hui Li^{a,b}, Adriana Christine Panayi^{c,f}, Michael Alfertshofer^g, Bong-Sung Kim^h, Weixian Hu^{a,b}, Yanzhi Zhao^{a,b}, Qian Feng^{d,*}, Yuval Rinkevich^{e,*}, Bobin Mi^{a,b,**}, Guohui Liu^{a,b,**}

^a Department of Orthopaedics, Union Hospital, Tongji Medical College, Huazhong University of Science and Technology, Wuhan 430022, PR China

^b Hubei Province Key Laboratory of Oral and Maxillofacial Development and Regeneration, Wuhan 430022, China

^c Division of Plastic Surgery, Brigham and Women's Hospital, Harvard Medical School, Boston, MA, 02152, USA

^d Key Laboratory of Biorheological Science and Technology, Ministry of Education College of Bioengineering, Chongqing University, Chongqing 400044, PR China

^e Institute of Regenerative Biology and Medicine, Helmholtz Zentrum München, Max-Lebsche-Platz 31, 81377 Munich, Germany

^f Department of Hand, Plastic and Reconstructive Surgery, Microsurgery, Burn Center, BG Trauma Center Ludwigshafen, University of Heidelberg, Ludwig-Guttman-Strasse 13, 67071 Ludwigshafen/Rhine, Germany

^g Department of Plastic Surgery and Hand Surgery, Klinikum Rechts der Isar, Technical University of Munich, Munich, Germany

^h Department of Plastic Surgery and Hand Surgery, University Hospital, Zurich, Switzerland

ARTICLE INFO

Keywords:

Biomaterials

Wound healing

Diabetic wound healing

Hydrogels

Efferocytosis

Macrophage reprogramming

ABSTRACT

Efferocytosis is a critical process whereby macrophages residing in the wound area play a key role in the efficient clearing and degradation of apoptotic neutrophils. This process is followed by a phenotypic transition toward an anti-inflammatory state, essential for inflammation resolution and tissue repair. The cystine/glutamate antiporter SLC7A11 has recently been identified as an inhibitor of efferocytosis, and its blockade has been found to enhance wound healing. In this study, we demonstrated that tiliroside, a plant-derived glycoside containing flavones, binds directly to SLC7A11 and pyruvate kinase isozyme M2 (PKM2). This was established by molecular docking predictions and activity-based protein profiling (ABPP). Cytological experiments revealed that tiliroside promoted the process of efferocytosis and led to glycolysis-related macrophage reprogramming. To facilitate targeted drug delivery to macrophages at diabetic wound sites, we designed a novel hybrid biomaterial. This hybrid biomaterial, prepared as Gel@Til iRGD&PS@PLGA NPs is manufactured by loading tiliroside (Til)-conjugated iRGD&PS double modified lipid nanoparticles (iRGD&PS@PLGA NPs) into a pH-responsive hydrogel matrix. The administration of Gel@Til iRGD&PS@PLGA NPs in diabetic cutaneous wound models has been shown to significantly promote tissue regeneration through the promotion of efferocytosis and glycolysis-related macrophage reprogramming. Therefore, this study introduces a novel approach to diabetic wound management by leveraging the promotion of efferocytosis.

1. Introduction

Diabetes mellitus, a pathological condition of the endocrine system marked by significantly elevated levels of glucose in the bloodstream, persist as some of the most widespread and swiftly escalating health

issues globally [1]. The complications that emerge from prolonged diabetes includes, but is not limited to major vascular, renal, and neurologic complications [1,2]. Diabetic foot ulceration stands out as a particularly grave consequence of diabetes, affecting an estimated 18.6 million individuals across the globe. Diabetic foot ulcers precede

* Corresponding author.

** Corresponding author at: Department of Orthopaedics, Union Hospital, Tongji Medical College, Huazhong University of Science and Technology, Wuhan 430022, China.

E-mail addresses: qianfeng@cqu.edu.cn (Q. Feng), yuval.rinkevich@helmholtz-munich.de (Y. Rinkevich), mibobin@hust.edu.cn (B. Mi), liuguohui@hust.edu.cn (G. Liu).

<https://doi.org/10.1016/j.cej.2024.154800>

Received 11 June 2024; Received in revised form 25 July 2024; Accepted 11 August 2024

Available online 13 August 2024

1385-8947/© 2024 The Authors. Published by Elsevier B.V. This is an open access article under the CC BY-NC license (<http://creativecommons.org/licenses/by-nc/4.0/>).

approximately a precursor to about 80 % of amputations performed on the lower limbs of individuals with diabetes, and they are also linked to a higher mortality rate [3–5]. These ulcers exhibit numerous pathological alterations within the tissue's microenvironment, such as prolonged inflammation, alterations in angiogenesis, dysregulation of matrix deposition, impairment of neuropeptide signaling, cell senescence, increase in propensity for bacterial infections and biofilm formation, wound hypoxia and neuropathy [6–8]. Tackling these detrimental factors and fostering a conducive microenvironment for the repair of diabetic wounds remain a major challenge [8].

The regulation of the inflammation phase in the wound healing process for the treatment of diabetic wounds has recently aroused a significant amount of attention [7]. The natural process of healing wounds involves a complex series of cellular and molecular events that occur in distinct, yet overlapping stages: initial hemostasis, inflammation, proliferation and ultimately remodeling [9,10]. However, the healing process in chronic diabetic wounds is marked by a failure in this orderly progression, particularly in moving from the inflammation phase to the cell proliferation phase [11]. Inflammation, a critical process involving neutrophils, monocytes, and macrophages, is tightly regulated to eliminate pathogens and remove damaged tissue to ultimately restore tissue homeostasis [12–14]. Neutrophils are typically the first leukocytes that are recruited to wound sites at the early stage of inflammation to clear debris and eliminate pathogens [15]. Following the release of tissue damage products, neutrophil numbers decrease in the wound site to conclude the inflammation phase [16,17]. The process of neutrophil clearance, mainly through apoptosis and their subsequent consumption by macrophages, is known as efferocytosis [18]. This process aids in shifting macrophages from a proinflammatory to an anti-inflammatory state, crucial for tissue homeostasis restoration and regeneration [19,20]. Nevertheless, slow-healing diabetic wounds are characterized by large numbers of persistent neutrophils, leading to the degradation of newly formed collagen and impairment of tissue repair [6,7,21]. Additionally, the persistence of proinflammatory macrophages (M1) at the diabetic wound site also has been associated with impaired wound healing [22]. Hence, strategies to ameliorate efferocytosis and promote macrophage transition towards anti-inflammation could be key in enhancing tissue regeneration and healing of slow-healing diabetic wounds.

Several significant targets linking to the efferocytosis have aroused increasingly attention. PKM2 has been found as one of the regulators in efferocytosis. Genetic deletion of PKM2 in myeloid cells or limiting its nuclear translocation results in boosting efferocytosis and suppressing inflammation [23]. Another previous study by Maschalidi et al. [24] has demonstrated the role of the membrane transporter SLC7A11 in the regulation of efferocytosis in diabetic wound healing. Elevated expressions of SLC7A11 were observed in the wounds of diabetes-susceptible db/db mice, and interventions targeting SLC7A11 were shown to expedite wound healing [24,25]. Further investigations indicated that the blockade of SLC7A11 pharmacologically, or its downregulation/elimination through small interfering RNA (siRNA), markedly improved efferocytosis in dendritic cells [24]. However, it remains elusive whether PKM2 or SLC7A11 shows a similar function in macrophages in diabetic wounds. Furthermore, additional research is required to identify the best approach to regulate PKM2 or SLC7A11 in diabetic wounds.

The above-mentioned observations presented here indicate the possibility of alleviating the persistent inflammatory condition observed in diabetic wounds through the suppression of SLC7A11 and enzymes associated with aerobic glycolysis. Tiliroside (Til), a glycoside of plant origin that includes flavones, demonstrates promise as an agent that combats inflammation and has been documented to suppress SLC7A11 in prior research [26–28].

In this study, we delved deeper into the pharmacological effects and protein targets of Til utilizing both animal and cell culture models. We explored the effects of Til on macrophage efferocytosis and metabolic reprogramming, focusing on mechanisms that have not been previously

explored. We performed molecular docking predictions and activity-based protein profiling (ABPP) to demonstrate that tiliroside directly binds to SLC7A11 and PKM2, resulting in an enhanced process of efferocytosis and transition of macrophages towards an anti-inflammatory state. During studying the mechanism of Til, we noticed that the PKM2/HIF-1 α pathway was inhibited, which has a promoting effect on angiogenesis. Hence, an appropriate approach needed to be explored to regulate PKM2/HIF-1 α pathway of macrophages with limited affection to endothelial cells. To achieve this, we developed a hybrid biomaterial designed to deliver tiliroside specifically to macrophages. Mechanically, Til was conjugated to iRGD&PS double-modified lipid nanoparticles (iRGD&PS@PLGA NPs), a nano-precipitation-self-assembly nanoparticles incorporating the cytotropic sequence iRGD and “eat me” signal molecule phosphatidylserine to specifically target macrophages. The iRGD&PS@PLGA NPs were then loaded into a pH-responsive hydrogel matrix, which showed pH-responsive release of NPs in inflammatory environment and was proposed to fuel the transition from the inflammation to the proliferation phase of the wound healing process. (Scheme 1).

2. Materials and methods

2.1. Materials

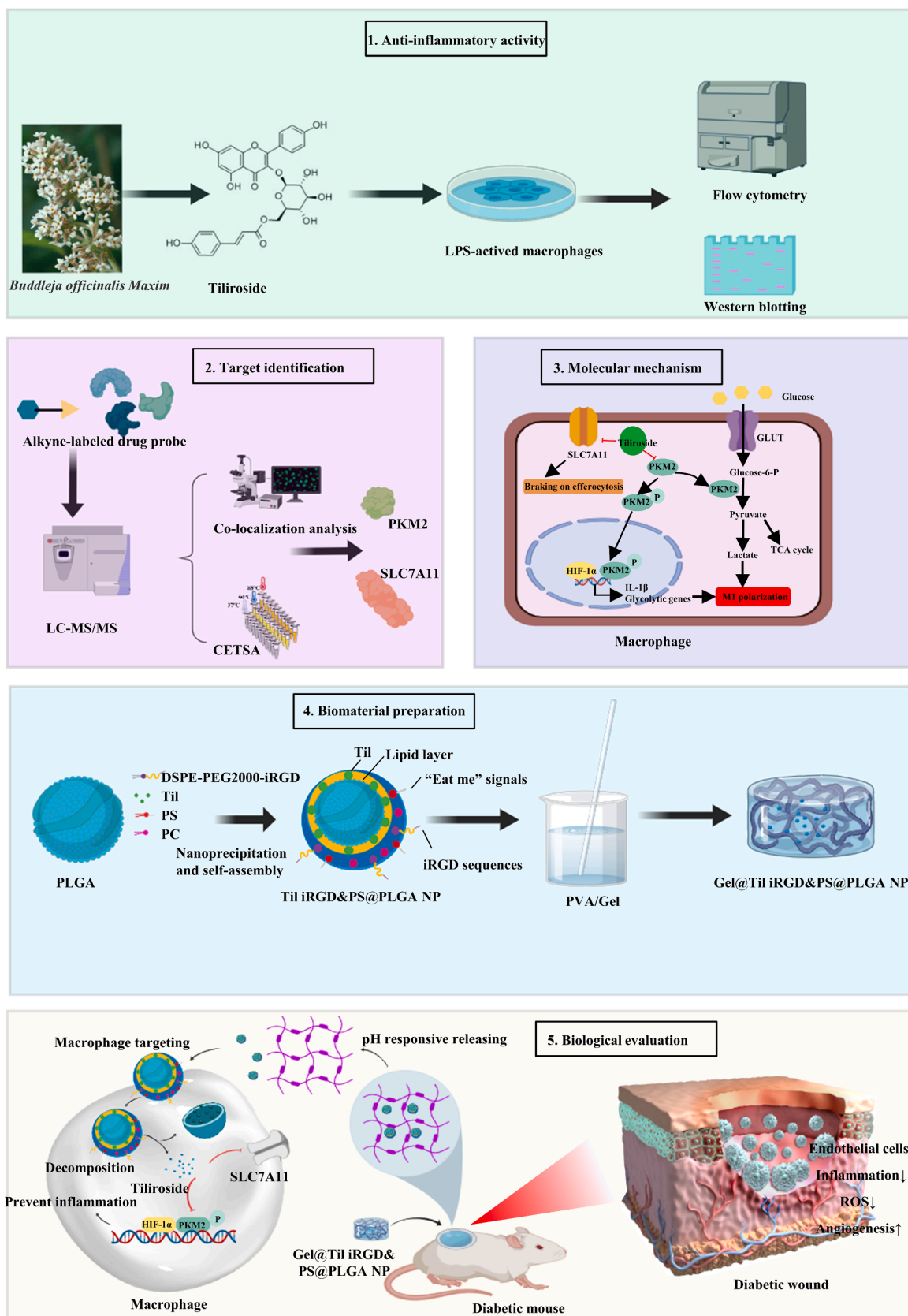
DSPE-PEG2000-iRGD and PS were purchased from Rulx Biological Technology (Xi'an, China). Sigma-Aldrich (Shanghai, China) provided Type A Gelatin from Porcine Skin, Til, PLGA and PVA. Gibco (Thermo Fisher Scientific Inc., Waltham, MA, USA) supplied the minimum necessary medium (MEM), fetal bovine serum (FBS), and penicillin–streptomycin. The aliquots were lyophilized and stored in -20°C .

2.2. Preparation of PVA/gelatin composite hydrogel

Hybrid gel formulations were prepared with various concentrations of gelatin (Aladdin, Shanghai) and PVA (Aladdin, Shanghai). In brief, PVA (10 g) was dissolved in 100 mL deionized water at 90°C , and different amounts of gelatin (0, 0.75, 1.50, 2.25, 3.00, 3.75 g) were then added to the solutions, followed by continuous stirring at 200 rpm for up to 30 min at 30°C , for complete mixing of the two solutes, until a clear solution formed. Next, it was poured into a test tube and left at room temperature until completely congealed. The congealed gels were taken from the test tube, cut into 5-millimeter-sized discs, and dried in a Petri dish at room temperature, resulting in PVA/gelatin composite hydrogels with different gelatin contents.

2.3. Synthesis and characterization of iRGD&PS double-modified lipid nanoparticles

A nano-precipitation-self-assembly method was used to prepare the functional lipid layer PLGA (Aladdin, Shanghai) nanoparticles (Til iRGD&PS@PLGA NP), at 65°C . Four mL acetonitrile (dissolved 4 mg of Til and 36 mg of PLGA) was rapidly injected into a 10 mL 5 % aqueous ethanol solution (dissolved 5 mg of DSPE-PEG2000-iRGD (Rulx Biological Technology, Xi'an) and 15 mg of brain-derived PS phospholipids (Rulx Biological Technology, Xi'an)). The mixture was stirred at 400 rpm for 8 h. The unencapsulated free drug in the nanoparticle solution was removed by an ultrafiltration centrifuge tube, and the drug particles were resuspended in pure water to a drug concentration of about 1 mg/mL for use. PLGA particles without drug or lipid layer modification were prepared by the same method for the experimental control group. An appropriate amount of Dil labeling dye was added to the acetonitrile solution to prepare fluorescently labeled PLGA nanoparticles.



Scheme 1. Schematic overview of diabetic wound healing processes promoted by Gel@Til iRGD&PS@PLGA NPs. (1) Til exhibits pro-inflammatory activity *in vitro*. (2) Til specifically interacts with PKM2 and SLC7A11 was evidenced by Activity-Based Protein Profiling (ABPP) and Cellular Thermal Shift Assay (CETSA) techniques (3) Til was proved to attenuates the inflammatory response and glycolytic activity in macrophages activated by inhibition of PKM2 function. (4) Preparation of Gel@Til iRGD&PS@PLGA NPs. (5) Regulation of the healing processes in diabetic wounds.

2.4. Preparation of nanoparticles-loaded PVA/gelatin hydrogel

PVA/gelatin mixed solution with 1.50 % (w/v) gelatin and 10 % (w/v) PVA was obtained according to the abovementioned protocol. Nanoparticles (0.5 % (w/v)) were added into the PVA/gelatin solution at 30°C under magnetic stirring. After continuous stirring at 200 rpm for up to 30 min, the composed solution was poured into a test tube and left at room temperature until completely congealed, ultimately resulting in the nanoparticles-loaded PVA/gelatin composite hydrogel.

2.5. Morphology characterization

The prepared hydrogel was subjected to rapid freezing using liquid nitrogen to maintain its structural integrity prior to lyophilization. For an in-depth analysis, the hydrogel underwent cross-sectioning after being uniformly coated with a gold layer, followed by morphological examination through transmission electron microscopy (TEM).

2.6. Fourier transform infrared spectroscopy (FT-IR)

The samples were combined with potassium bromide at a 1:100 ratio and subsequently compressed into pellets. Spectral data were acquired using the NICOLET 380 FTIR spectrometer (Adhoek International Technology, Beijing), which operated across a spectral range of 4000–400 cm^{-1} with a resolution of 1 cm^{-1} in the transmission mode.

2.7. pH-Responsive degradation studies

Hydrogel degradation tests were carried out by immersing the samples in PBS solutions (pH 5.5 and pH 7.4) at 37 °C. The dried hydrogels were immersed into a buffer solution with pH 5.0 or 7.4. Subsequently, the hydrogels were weighed after removing the excess buffer solution with filter paper and freeze-dry. The degradation ratio was determined with the following equation:

$$\text{Degradation ratio (\%)} = (W_d - W_t) / W_d \times 100$$

with “ W_t ” being the weight of swollen hydrogel in pH of 5.0 or 7.4 at a certain time interval. And “ W_d ” being weight of hydrogel at the beginning of the test.

2.8. Macrophage culture and viability assays

RAW264.7 cells, procured from the Chinese National Cell Bank (Beijing, China), were maintained in Dulbecco's Modified Eagle Medium supplemented with 10 % fetal bovine serum (FBS) and incubated at 37 °C within a controlled environment of 5 % CO_2 and 95 % humidity. These cells were allocated to 96-well plates at a cell density of 6×10^3 cells per well and left to adhere for 12 h. Subsequent to this period, either Tiliroside or its probe variant (Til-P, concentrations ranging from 0.1 to 4.0 $\mu\text{mol/L}$) was introduced to the culture, which then continued for an additional 24-hour incubation. The CCK-8 kit (Dojindo, Japan) was utilized to evaluate cell viability, adhering strictly to the guidelines provided by the manufacturer.

2.9. In vitro efferocytosis assay

Bone marrow-derived macrophages were harvested from male C57BL/6J mice aged 6 weeks. The bones were processed and centrifuged to extract the bone marrow cells into sterile PBS at pH 7.4. This bone marrow cell suspension was then purified with PBS and cultured in DMEM enriched with 10 ng/ml M-CSF (Peprotech Inc, 315–02). On the fifth day of cultivation, cells were dislodged from the culture dishes using TBS containing 5 mM EDTA, re-suspended in fresh DMEM, and distributed into 24-well plates (3422, Corning, USA) at a rate of 0.18×10^6 cells per well. Dil-labeled apoptotic cells (ACs) were then incubated with the macrophages for 45 min at a 5:1 ratio of ACs to macrophages,

followed by triple washing with PBS. Forty-five minutes later, macrophages were washed again three times with PBS to discard any non-adherent ACs. Subsequently, the macrophages were fixed using 4 % formaldehyde for 20 min, stained with DAPI for 5 min, rinsed thrice with PBS, and visualized under a microscope (IX53, Olympus, Japan).

2.10. RAW264.7 transduction

Transfecting in RAW264.7 cells was used Lipofectamine LTX Reagent (Cat #: A12621, Thermo Fisher Scientific) following manufacturer's instructions. Plasmids were purchased from Genechem for PKM2 overexpression. Likewise, PKM2 in cells were detected by transfected with PKM2 siRNA (Tsingke Biotechnology, Wuhan). The siRNA sequences of Mouse PKM2 are as follows:

Sense (5'-3'), GAUCUGUGGAGAUGCUGAAGG,
antisense (5'-3'), UUCAGCAUCUCCACAGAUCGG.

2.11. Flow cytometric analysis

For macrophage polarization evaluation, antibodies for the study were procured from eBioscience. Initially, cells underwent incubation with FITC-labeled anti-CD11b, APC-conjugated anti-F4/80, and PE-tagged anti-CD86 antibodies for a duration of 30 min at a temperature of 4 °C. Subsequently, the cells were made permeable and labeled with PerCP/Cyanine5.5 conjugated anti-CD206 antibody for another 30 min at 4 °C. The cells were then cleansed with chilled PBS and their fluorescence was assessed using a specialized analyzer.

For efferocytosis evaluation, neutrophils were undergoing UV-treated for 30 min to induce apoptosis and were labeled with Dil for 30 min, and then incubated at 37°C for 4 h. After incubation, apoptotic cells were co cultured with BMDMs for 45 min at a ratio of 5:1. non-engulfed cells were removed, and BMDMs were washed with PBS. F4/80-positive and Dil-positive BMDMs were detected using flow cytometry.

2.12. mRNA expression in in vitro cultured cells

To isolate total RNA from the cells, TRIzol® reagent was utilized. The extracted RNA was then reverse-transcribed into cDNA using HiScript III RT SuperMix (Vazyme, China), followed by quantification with 2x SYBR Green qPCR Mix (Invitrogen) and specific primer sets (Supplementary Table 3). β -actin was employed as a reference gene. Data were analyzed employing the $\Delta\Delta\text{Ct}$ method.

2.13. Protein expression in in vitro cultured cells

Cell samples were disrupted in a buffer containing 1 % of both protease and phosphatase inhibitors (NCM Biotech, Suzhou). Following separation via SDS-PAGE, the proteins were transferred to nitrocellulose (NC) membranes supplied by Millipore. These membranes were subsequently incubated with 5 % skim milk to block non-specific binding sites for one hour, followed by an overnight incubation at 4 °C with specific primary antibodies directed against Arg1, iNOS, IL-1 β (Proteintech Group, Wuhan), PKM2, SLC7LA11, HIF-1 alpha (ABclonal, Wuhan), and β -actin (procured from Abcam, UK). The membranes were then incubated with horseradish peroxidase (HRP)-conjugated secondary antibodies (Aspen) at 4 °C for four hours. The immunoblots were detected and imaged using the ChemiDoc XRS+System by Bio-Rad.

2.14. Protein labeling in situ and in vitro

Proteomic labeling in situ within RAW264.7 cells under cultivation was successfully achieved, with the methodology for ABPP illustrated in Fig. 3a. Briefly, RAW264.7 cells were incubated for 24 h with LPS at a dose of 100 ng/ml, subsequently exposed for 2 h to either Til-P or DMSO. Following these treatments, proteins from the cells were thoroughly extracted. A freshly prepared clickable reaction mixture, containing 100

$\mu\text{mol/L}$ Tris (3-hydroxypropyltriazolylmethyl) amine (THPTA), 1 mmol/L sodium ascorbate (NaVc), 50 $\mu\text{mol/L}$ TAMRA-azide, and 1 mmol/L CuSO_4 , was added in equal volumes to the protein extracts. This concoction was incubated for 2 h at room temperature. Protein precipitation was induced by adding acetone chilled to $-20\text{ }^\circ\text{C}$, with the precipitated proteins subsequently resolubilized in 50 μl of $1 \times$ loading buffer via sonication and heated for 12 min at $95\text{ }^\circ\text{C}$. Protein separation was conducted using 10 % SDS-PAGE, and Til-P labeled proteins were detected using Azure Sapphire (RGB-NIR, USA). Following separation, protein gels were stained with Coomassie Brilliant Stain provided by Abcam, Cambridge, UK. For the *in vitro* labeling of purified recombinant proteins, a 60-minute room temperature incubation with Til-P in PBS was performed, followed by addition to the clickable reaction mixture and another 2-hour incubation at room temperature. The proteins were then separated by SDS-PAGE and visualized with Azure Sapphire RGBNIR. In competitive protein labeling experiments, cells or proteins were first treated with competitors for 30 min before a 60-minute incubation with Til-P. The click chemistry reaction and electrophoresis were then carried out as described above.

2.15. ABPP-based identification of targets

RAW264.7 cells were activated using LPS for 24 h, then treated for an additional 30 min with or without Til, followed by a 2-hour exposure to either Til-P or DMSO. Post-treatment, proteins were extracted, quantified via the BCA protein assay, and subjected to click chemistry reactions for 2 h at room temperature. Proteins were then precipitated using acetone chilled to $-20\text{ }^\circ\text{C}$, redissolved in PBS containing 1.5 % SDS, and incubated with streptavidin-coated beads for 4 h at room temperature. The azide-functionalized magnetic beads were thoroughly washed with PBS containing 1 % SDS (twice), 0.1 % SDS (once), 6 mol/L urea (three times), and then PBS (twice). The proteins bound to the azide magnetic beads were eluted, separated by SDS-PAGE, and the bands of interest were excised, finely minced, reduced with dithiothreitol (DTT), alkylated with iodoacetamide (IAA), and digested with trypsin overnight at room temperature. The resulting peptides were purified using a C18 column, labeled with TMT reagents (Thermo Scientific, MA, USA), and identified via liquid chromatography-tandem mass spectrometry (Orbitrap Fusion Lumos, Thermo Scientific, MA, USA). The proteins bound to azide magnetic beads, after being separated by SDS-PAGE as described, were also analyzed through Western blotting for further examination.

2.16. Cellular thermal shift assay

RAW264.7 cells, activated by LPS, were lysed on ice for 30 min, allowing for the extraction of total protein. Subsequently, equal volumes of protein solution (2 mg/ml, 1 ml) were incubated with either Til (20 $\mu\text{mol/L}$) or DMSO at room temperature, for a duration of 50 to 60 min. These solutions were then evenly divided into 10 PCR tubes and exposed to a temperature gradient for 3 min at 10 different settings, followed by a cooling period at $4\text{ }^\circ\text{C}$ for 3 min, utilizing a thermal cycler (Applied Biosystems, Thermo Scientific). After the heating process, samples were centrifuged at $20,000 \times g$ for 10 min, mixed with $1 \times$ loading buffer, heated at $95\text{ }^\circ\text{C}$ for 10 min, and subjected to Western blot analysis for protein detection.

2.17. Drug affinity responsive target stability approach

The DARTS method was employed to pinpoint drug affinity-responsive targets. RAW 264.7 cells were lysed using a buffer formulated for immunoprecipitation (20 mM Tris-HCl at pH 7.5, 150 mM NaCl, 1.5 mM MgCl_2 , 2 mM EDTA, and 0.5 % NP-40), which was enhanced with a protease inhibitor cocktail provided by Roche. Following this, the lysates were treated with TNC buffer (50 mM Tris-HCl at pH 8.0, 50 mM NaCl, and 10 mM CaCl_2), and protein

concentrations were determined. These lysates were then incubated with various concentrations of Til or DMSO (serving as the control) for one hour at room temperature. Pronase from Coolaber was used for proteolysis at a ratio of 2000:1 for 30 min at room temperature. The proteolytic reaction was stopped by the addition of SDS-PAGE loading buffer, and the proteins were denatured by heating at $100\text{ }^\circ\text{C}$ for 10 min before being subject to Western blot analysis. The band intensities for PKM2 and SLC7A11 were quantified using ImageJ software.

2.18. Molecular docking of Til with potential protein targets

The molecular configuration of Til was retrieved from the PubChem database, while the three-dimensional conformations of PKM2 (PDB ID: 8HGF) and SLC7A11 (PDB ID: 7CCS) were sourced from the RCSB Protein Data Bank. The process of integrating water and hydrogen atoms into the protein structures was accomplished using Discovery Studio Client. Subsequently, Til's docking onto these molecular structures was performed employing a combination of AutoDock Tools, AutoDock Vina, and Pyrx-0.8. The outcomes of the docking procedures were examined and rendered using Pymol for visualization purposes. The docking scores and two-dimensional and 3D pose views were generated for further analysis of the interaction of Til with PKM2 and the associated binding affinities.

2.19. Protein purification

The procedures for purifying proteins and the related experimental setup are illustrated in [Supplementary Fig 3c](#). DNA sequences encoding the human wild-type pyruvate kinase M2 (PKM2) isoform (GenBank Accession number NP_002645.3) and its Arg120Cys mutant were cloned into the pET-28a vector (obtained from Genechem, China). In a similar fashion, the sequences for human SLC7A11 (GenBank Accession number NP_000004.12) and its Glu159Val variant were also cloned into the pET-28a vector (Genechem, Shanghai). These prepared vectors were subsequently transformed into *E. coli* BL21 cells. Protein expression was induced by adding 0.4 mmol/L isopropyl- β -D-1-thiogalactopyranoside for 12 h at a temperature of $16\text{ }^\circ\text{C}$. Following induction, the bacterial cells were collected and lysed in a lysis buffer that included 20 mmol/L Tris-HCl, 200 mmol/L NaCl, and 1 mmol/L PMSF at a pH of 8.0. The recombinant proteins were then purified through Ni-NTA affinity chromatography (MCE, China), eluted with imidazole, and concentrated using centrifugal filter units. The purity and conformation of the isolated proteins were verified by Coomassie Brilliant Blue staining.

2.20. Co-immunoprecipitation (co-IP) assay

RAW264.7 cells were cultured in 10 cm plates and subsequently exposed to 40 μM Til for a duration of 24 h. Lysis of these cells was achieved at $4\text{ }^\circ\text{C}$ using ice-cold IP Lysis/Wash Buffer that included protease inhibitors. The co-IP analysis proceeded with the utilization of the Pierce Co-immunoprecipitation Kit (Thermo Scientific, Waltham, MA, USA), adhering to the instructions provided by the manufacturer.

2.21. Cytocompatibility evaluation of Gel@Til iRGD&PS@PLGA NPs

To ascertain the viability of HUVECs incubated in RPMI 1640 medium containing the extract from the hybrid biomaterial hydrogel, the Calcein-AM/PI double staining kit (Sigma-Aldrich) was employed. Fluorescence microscopy images were captured at 24, 48, and 72-hour intervals using an IX53 microscope (Olympus, Japan).

2.22. Transwell assays

MAECs, sourced from the Chinese National Cell Bank (Beijing, China), were grown in RPMI 1640 medium enriched with 10 % FBS at $37\text{ }^\circ\text{C}$. Approximately 5×10^4 MAECs in FBS-free medium were seeded

into the upper compartments of 24-well transwell plates (3422, Corning, USA). The lower compartments were supplemented with 600 μ L of medium containing FBS to serve as a chemoattractant. Following a 24-hour incubation period, the cells were rinsed thrice with PBS, fixed in 4 % paraformaldehyde for 30 min, and stained with 0.5 % crystal violet for another 30 min. Non-migratory or non-invasive cells were removed using sterile cotton swabs. For each well, three random fields were imaged under a bright field microscope.

2.23. Scratch-wound healing assays

MAECs were seeded into 6-well plates until they reached 90–100 % confluence. A sterile 200- μ L pipette tip was employed to create a cross-shaped scratch on the cell monolayer. PBS was utilized to wash away any detached cells. The progress of wound closure was documented at 0 h, 12 h, 24 h, and 36 h using an inverted microscope (IX53, Olympus, Japan).

2.24. Tube formation assay

In a 96-well plate coated with Matrigel, MAECs (2×10^4 cells/well) were distributed and allowed to adhere for 45 min, followed by an additional incubation period of 6 h. Tube formation was observed in three randomly selected fields under an inverted microscope, with the quantification of branch points and tube lengths being performed using ImageJ software.

2.25. Generation of diabetic mice

The development of a diabetic mouse model was performed with the authorization of the Institutional Animal Care and Use Committee at Tongji Medical College, Huazhong University of Science and Technology (IACUC Number: 2523). Six-week-old male C57BL/6J mice were placed on a high-fat diet for four weeks, then received daily intraperitoneal injections of streptozotocin (STZ; 40 mg/kg) over a period of seven days. Mice that displayed fasting blood glucose levels above 16.7 mmol/L in three successive measurements were identified as having diabetes mellitus and were chosen for further research.

2.26. Diabetic chronic wound healing in vivo

Diabetic mice, induced by STZ, were sedated using intraperitoneal injections of pentobarbital sodium (50 mg/kg; Sigma Aldrich). On their backs, full-thickness skin wounds measuring 1.0×1.0 cm were created. These mice were then randomly assigned into groups, each receiving 200 μ L of the experimental sample on days 0, 3, 5, 7, 10, and 14 post-wound creation ($n = 8$). The wounds were covered with transparent dressings (Tegaderm™ Film) and were documented and measured using a caliper on days 0, 3, 5, 7, 10, and 14. Wound closure rates were analyzed using ImageJ software as follows:

$C_n = (A_0 - A_n) / A_0 \times 100\%$ with “ C_n ” being the percentage reduction of the wound area on the respective days; “ A_0 ” being the size of the original wound; and “ A_n ” being the area of the wound on the respective day after the injury.

2.27. Histological, Masson, immunohistochemical, and immunofluorescent staining

Tissue samples from mouse skin wounds were preserved in 4 % paraformaldehyde, encased in paraffin wax, and sectioned into slices 4 μ m in thickness. These sections underwent staining processes with either Hematoxylin and Eosin or Masson’s trichrome and were subsequently visualized utilizing a PANNORAMIC Flash series digital scanner (3DHISTECH, Hungary).

On the 14th day post-wounding, the mice were euthanized, and the wound tissues were processed for paraffin embedding and then

subjected to CD31 staining. Antigen unmasking was carried out in citrate buffer for 15 min, succeeded by a 30-minute blocking phase in goat serum. Overnight incubation at 4 °C with anti-CD31 antibodies (dilution 1:100; Abcam) was followed by PBS washes, and staining with DAB and counterstaining with hematoxylin. Microvascularization assessment at the wound locations was conducted via a microscope (IX53, Olympus, Japan), through counting CD31 + cells across five visual fields. Vessels were specifically identified as those having 2 to 10 μ m in diameter.

For the detection of macrophages, immunohistochemical analyses were conducted using antibodies against Arg1 and iNOS. Observations of the treated sections were made using either an Olympus CX31 optical microscope (Tokyo, Japan) or a Zeiss fluorescence microscope (Jena, Germany). The antibodies for Arg1 and iNOS were sourced from Abcam (Cambridge, Britain).

2.28. In vivo efferocytosis assay

On day 7, mice were euthanized and their wound tissues collected. These tissues underwent a process of formalin fixation, embedding in paraffin, and then slicing. The resultant slices (5 μ m thick) were then stained using a neutrophil-specific antibody (LY6G) and a macrophage-specific antibody (F4/80). The assessment of efferocytosis in situ involved the enumeration of DAPI-stained nuclei that either were in proximity to macrophages, suggesting efferocytosis (“associated”), or remained distant from macrophages (“free”). Cells undergoing apoptosis and found near macrophages were categorized as being associated with macrophages. Conversely, apoptotic cells lacking contact with adjacent macrophages were classified as free.

2.29. DHE staining

Subsequent to their sacrifice on day 7, wound tissues from mice were extracted. The evaluation of intracellular ROS was conducted using the DHE ROS indicator (5 μ m), which was applied for 10 min followed by three PBS washes. The imaging of these tissues was performed using the IX53 microscope.

2.30. Extracellular acidification rate (ECAR) assay

Metabolic changes in extracellular acidification rate of RAW 264.7 cells were measured using the Seahorse XFe96 Analyzer. In the beginning, inoculate 10,000 RAW 264.7 cells of different groups into Seahorse XFe96 cell-specific culture plates. Then cells were stimulated for 24 h with/without the addition of 100 ng/mL LPS. 30 min before the ECAR test, the medium was replaced with a special medium containing 2 mM glutamine. For the OCR assay, the assay medium was supplemented with 2 mM glutamine, 1 mM sodium pyruvate, and 10 mM glucose. The cell culture plates were placed in a 37 °C non-co2 incubator for 1 h prior to the final assay. ECAR were measured using the Seahorse XFe96 Analyser (Agilent).

2.31. Statistical analysis

Statistical analyses were performed using GraphPad Prism (version 8.2.1) and ImageJ (version 2.1.0) software. Data were compiled from a minimum of three separate experiments, each containing at least three replicates under each condition. Results are presented as mean \pm standard deviations (SDs). The Student’s *t*-test was employed to assess differences between two groups, with significance denoted as follows: * $P < 0.05$, ** $P < 0.01$, *** $P < 0.001$, and **** $P < 0.0001$.

3. Results and discussion

3.1. Anti-inflammatory effects of tiliroside

Firstly, we evaluated whether Til could serve as a viable

pharmacological agent for enhancing efferocytosis and facilitating the anti-inflammatory reprogramming of macrophages. To evaluate the effects of Til in anti-inflammation, we performed flow cytometry and western blotting assay. In LPS-activated macrophages, Til treatment downregulated the proinflammatory biomarker CD86 and upregulated anti-inflammatory biomarker CD206 in LPS-activated macrophages. (Fig. 1a, b, c, d) The results of western blotting also showed that Til did significantly affect the expression of Arg1 and iNOS, indicating the promotion of transition towards an anti-inflammatory state in LPS-activated macrophages (Fig. 1e, f).

To explore the impact of Til on efferocytosis, neutrophils (stained red) were treated with 800 μ M PA for 24 h to trigger apoptosis. Then, these cells were cocultured with macrophages (stained in blue) treated with 40 μ M Til or not. Til-treated macrophages showed a significant increase in efferocytosis (Fig. 1g, h). Then we performed flow cytometry to further quantify the efferocytosis ability of macrophages. Dil was used to label ACs. Compared with the control group, Til significantly promoted efferocytosis of macrophages (Fig. 1i, j). These outcomes demonstrate Til's potential in modulating efferocytosis and the anti-inflammatory reprogramming of macrophages.

Data from the World Health Organization (WHO) forecast a surge in global diabetes incidence, expected to escalate from 171 million cases in 2010 to 366 million by 2030. This anticipated increase in diabetes prevalence is associated with a rise in related complications, such as foot ulcers [29]. Consequently, there is an urgent need for innovative therapeutic strategies to promote wound healing in diabetic patients, ultimately aiming to improve quality of life and reduce morbidity and mortality. In the realm of potential anti-diabetic treatments, flavonoids have recently drawn considerable interest. Derived from plants, flavonoids exhibit a broad spectrum of biological functions, including anti-diabetic, anti-inflammatory, antibacterial, and antioxidant properties [30]. As a traditional anti-inflammatory drug, tiliroside, a flavonoid contained in various edible plants or specific plant parts (e.g., fruits, leaves, or roots), has been found to exhibit anti-inflammatory properties in previous studies, both *in vivo* and *in vitro* [31]. *In vitro*, tiliroside has been reported to inhibit the production of TNF- α , iNOS, and IL-6 in LPS-stimulated RAW264.7 and BV2 microglia [32,33]. However, the effects of tiliroside on diabetic wound healing and the underlying mechanisms still remained elusive. In this part, we proved the anti-inflammatory and promoting efferocytosis effects of tiliroside, which indicates the potential application in diabetic wound healing.

3.2. Tiliroside binding to PKM2 and SLC7A11

To elucidate the role of Til in facilitating efferocytosis and steering macrophages towards an anti-inflammatory phenotype, we engaged in activity-based protein profiling (ABPP) studies to pinpoint potential protein targets within LPS-stimulated macrophages.

ABPP serves as a widely adopted technique for identifying drug targets, utilizing cell-penetrating probes for the visualization of tagged proteins [34]. This method allows for the formation of stable probe-protein complexes *in situ*, facilitating subsequent protein isolation and proteomic analysis to decipher the drug's mechanism of action [35]. In conducting ABPP experiments, a tiliroside-probe (Til-P) featuring a clickable alkyne tag was synthesized. Mass spectrometry analysis validated the accurate synthesis of Til-P, as depicted in Supplementary Fig 1a and b. CCK8 tests showed that the inhibitory effects of Til-P were comparable to those of Til (Supplementary Fig 1c). We incubated LPS-activated macrophages with Til-P, and the proteins subsequently labeled by Til-P were click-conjugated to the fluorescent dye FAM-azide (Supplementary Fig 1d). The specificity of Til-P binding was confirmed by showing that free Til competed effectively with Til-P for fluorescent labeling (Supplementary Fig 1e). Using a fluorescently labeled Til-P, we found that the probe was distributed throughout the cell (Supplementary Fig 1f), enabling a thorough investigation of intracellular protein targets for Tiliroside.

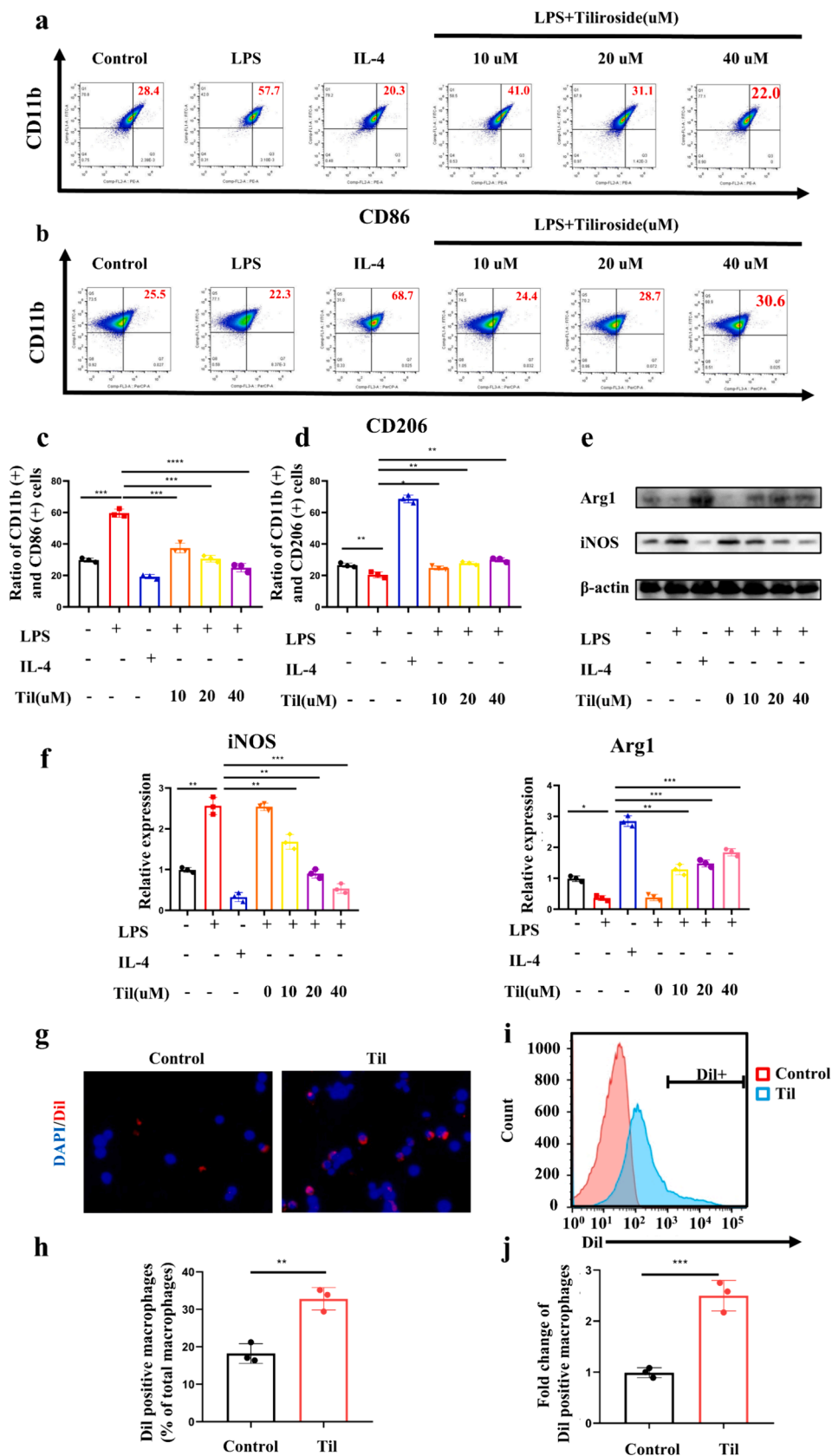
Following the synthesis and validation of Til-P's functionality, we then performed ABPP to explore the targets of Til and its underlying mechanisms. As illustrated in the flow diagram, proteins interacting with Til-P underwent click chemistry with azide beads for enrichment, subsequent separation via SDS-PAGE, and identification through LC-MS/MS (Fig. 2a). Total Ion Current (TIC) results from the mass spectrometry indicated a lower protein abundance in the control group not treated with Til-P (Fig. 2b), in contrast to the significantly enriched protein abundance in the Til-P treated group (Fig. 2c). This finding implies that the presence of FAM-azide beads alone does not suffice for protein isolation. Yet, the combination of FAM-azide beads and Til-P through a click-reaction effectively isolates Til-associated target proteins. Proteins identified by LC-MS/MS are summarized in Fig. 2d. Of all proteins identified, subsequent analyses were performed for proteins reported to regulate efferocytosis and inflammation such as PKM and SLC7A11. PKM (subtype 2), a crucial enzyme in glycolysis, can shift to the nucleus in its monomeric and dimeric forms, interacting with Hif-1 α to modulate the expression of pro-glycolytic enzymes and promoting the transition of macrophages towards the M1 phenotype [36]. Doddapattar et al. [23] have also highlighted that PKM2 deletion enhances efferocytosis in myeloid cells. Similarly, the membrane transporter SLC7A11 is recognized as inhibiting efferocytosis, with its removal or silencing improving efferocytosis in dendritic cells [25]. To further explore the functions of Til, we performed western blotting assay to evaluate its underlying targets. In macrophages stimulated with LPS, Til did not markedly alter PKM1 expression but did moderately decrease the LPS-induced elevation of PKM2 and SLC7A11 expressions in a concentration-dependent manner (Fig. 2e, f). Together, these results strongly suggest that in LPS-activated macrophages, PKM2 and SLC7A11 might be the targets of Til, and their expression can also be regulated by Til.

3.3. Efferocytosis promotion and glycolysis-related transitioning of macrophages through til-induced inhibition of PKM2 signaling

Subsequently, our investigation delved into whether Til enhances efferocytosis by interacting with the PKM2-dependent signaling pathway. As a crucial target for Til, silencing PKM2 markedly reduced the level of the pro-inflammatory marker CD86 while increasing the expression of the anti-inflammatory marker CD206 in LPS-activated macrophages (Fig. 3a, b, c, d). The results of western blotting also showed that knocking down PKM2 significantly affect the expression of Arg1 and iNOS, indicating the promotion of transition towards an anti-inflammatory state in LPS-activated macrophages (Fig. 3e, f). Fluorescent images showed that knocking down PKM2 showed a significant increase in efferocytosis (Fig. 3g, h). Then we performed flow cytometry to further quantify the efferocytosis ability of macrophages. Dil was used to label ACs. Compared with the control group, knocking down PKM2 significantly promoted efferocytosis of macrophages (Fig. 3i, j).

Then, we further explore the underlying mechanisms of Til in regulating glycolysis and macrophage polarization. From the molecular mechanism, this knockdown significantly inhibited PKM2/HIF-1 α pathway and downregulated the expression of glycolysis-related genes (Fig. 4a-c). Next, the Seahorse Extracellular Flux analyzer was used to analyze bioenergetic function in macrophages. As shown in Fig. 4d-e, results from Seahorse glucose stress tests indicated that knocking down PKM2 or using Til could decreased the extracellular acidification rate (ECAR) in macrophages.

In this part, we further validated the direct targets of Til identified in Fig. 2 through cell-based experiments, demonstrating that Til inhibits destructive inflammatory responses via these targets. PKM2 is a key player involved in inflammatory processes [37]. Our findings in Fig. 1 revealed that Til significantly reduced inflammatory of macrophages activated by LPS. This reduction might be partially mediated by the suppression of PKM2 activity. Supporting this hypothesis, our data show that PKM2 deactivation leads to lowered IL-1 β levels and reduced



(caption on next page)

Fig. 1. Til improves efferocytosis and promotes the transition of macrophages towards an anti-inflammatory state. Representative flow cytometry of (a) CD86 + cells and (b) CD206 + cells. (c) The percentage of M1 phenotypes was quantified as the ratio of CD86 + and CD11b + cells (n = 3). (d) The percentage of M2 phenotypes was quantified as the ratio of CD206 + and CD11b + cells (n = 3). (e) RAW264.7 cells were treated with different concentrations of Til (0, 10, 20, 40 μM). Representative Western blot of Arg1 and iNOS levels in RAW264.7 cells in the presence of LPS (100 ng/mL). LPS-treated group (100 ng/mL) and IL-4 treated group (50 ng/mL) were used as positive and negative controls. (f) Quantitative analysis of iNOS and Arg1 protein levels in RAW264.7 cells (n = 3). (g) BMDMs and Til-treated RAW264.7 cells were incubated with Dil-labeled ACs at a time point of 30 min at a AC: RAW264.7 ratio of 5:1 (n = 3). (h) Percent efferocytosis was quantified as the number of macrophages with engulfed apoptotic cells as a percentage of total macrophages (n = 3). (i) Representative flow cytometry images for efferocytosis evaluation. (j) Quantification of Dil-positive BMDMs (n = 3). *P value < 0.05; **P value < 0.01; ***P value < 0.001 per; ****P value < 0.0001 per group by unpaired t test.

aerobic glycolysis, consistent with the findings of Xie et al [38]. This aligns with existing evidence that aerobic glycolysis enhances the expression of genes involved in inflammatory responses, leading to increased secretion of TNF- α , IL-1 β , and IL-6 [38]. Therefore, Til's ability to attenuate inflammatory reactions may stem from its inhibition of PKM2 and related enzymes, subsequently reducing aerobic glycolysis.

Furthermore, our study effectively demonstrated that Til regulates cellular metabolism by inhibiting aerobic glycolysis in LPS-stimulated macrophages. At the molecular level, Til downregulated the mRNA expression of HIF-1 α -dependent glycolytic enzymes in macrophages. Previous reports indicate that elevated glucose treatment significantly enhances the expression of both PKM2 and HIF-1 α , reprogramming macrophage metabolism and triggering pro-inflammatory gene expression [39,40]. In LPS-induced macrophages, Til inhibited the PKM2-HIF-1 α signaling pathway and the activation of HIF-1 α -driven genes critical for metabolic reprogramming, including GLUT1, HK2, and LDHA. In summary, our results indicate that Til modulates the PKM2 pathway to reduce efferocytosis and inhibit glycolysis in LPS-activated macrophages.

3.4. Inhibition of PKM2 and SLC7A11 activities through tiliroside

To demonstrate the direct interaction between Til and its target proteins, PKM2 and SLC7A11, a series of experiments were conducted. In pull-down experiments, a binding between Til-P and PKM2 as well as SLC7A11, and this binding was outcompeted by excess Til (Fig. 5a, Supplementary Fig 2a). Supporting this observation, laser scanning confocal microscope revealed co-localization of PKM2 and SLC7A11 with Til-P (Fig. 5b, Supplementary Fig 2b). Additional validation was obtained from cell heat transfer analysis (CETSA) which showed that Til increased the thermal stability of PKM2 and SLC7A11 (Fig. 5c,d, Supplementary Fig 2c, d).

Subsequently, our investigation focused on identifying potential interaction sites of Tiliroside (Til) within PKM2 and SLC7A11. Through molecular docking analyses, it was suggested that Til might interact with the Arg120 residue of PKM2 and the Glu159 residue of SLC7A11 within their substrate-binding regions (Fig. 5f and Supplementary Fig 2f). The potential docking sites were illustrated through virtual modeling (Supplementary Fig 3a, b). These results imply that Til specifically interacts with distinct amino acid residues in PKM2 and SLC7A11 within macrophages activated by LPS. Then, we utilized point mutation variations of the proteins to test, with mutating Arg120 to Cys in PKM2 and mutating Glu159 to Val in SLC7A11 led to decreased Til-P binding (Fig. 5g, Supplementary Fig 2g, Supplementary Table. 1, Supplementary Table. 2), suggesting that Til directly binds to PKM2 and SLC7A11.

To further confirm whether the binding between Til and PKM2 is required for the Til-mediated inhibition of PKM2, PKM2-silenced macrophages were transfected with wild-type PKM2 or the PKM2 Arg120-Cys mutant. Remarkably, exogenous Til treatment decreased the level of IL-1 β in macrophages transfected with the PKM2 WT, but not in those transfected with PKM2 mutant (Fig. 5h). The co-IP assay was then conducted to determine the relationship between PKM2 and HIF-1 α in HCC cell lines (Fig. 5i). The results showed that HIF-1 α were pulled-down by PKM2. The level of the PKM2/HIF-1 α complex in the Til-treated groups was lower than that in the Control groups, which suggested that Til mediated functions of PKM2 through inhibition the formation of PKM2/

HIF-1 α complex.

ABPP is a widely recognized method for discerning the cellular targets of natural compounds and small molecules [41]. In our study, we, our research utilized ABPP to reveal that Til can directly interact with PKM2 and SLC7A11 within macrophages activated by LPS. Our findings confirmed the selective interaction of Til with both PKM2 and SLC7A11 *in vitro* – as revealed by CETSA and co-localization experiments leading to the disruption of PKM2 activity as well as the PKM2-HIF-1 α signaling pathway in macrophages as shown by WB.

3.5. Preparation and characterization of Gel@Til iRGD&PS@PLGA NPs

Due to insufficient angiogenesis at diabetic wound sites, traditional drug delivery approaches, such as administration via the caudal vein, have been shown to be less effective in promoting diabetic wound healing [42]. To enhance drug delivery efficiency, we designed a PVA/gelatin hydrogel (abbreviated as Gel in the following) loaded with Til iRGD&PS@PLGA NPs (Gel@Til iRGD&PS@PLGA NPs). The hybrid biomaterial was constructed to precisely regulate efferocytosis and transition of macrophages towards an anti-inflammatory state in a two-stage approach, catering to both the initiation and resolution of inflammation. The initial stage involves the pH-responsive release of Til iRGD&PS@PLGA NPs from the hydrogel matrix in the acidic environment characteristic of inflammation. The second stage involves macrophage-targeted drug delivery.

Activation of PKM2/HIF-1 α pathway fuels M1 polarization of macrophages, while HIF-1 α pathway shows positive effects in angiogenesis process for endothelial cells [43]. An appropriate approach needs to be explored to regulate PKM2/HIF-1 α pathway of macrophages with less affection to endothelial cells. Hence, the Til iRGD&PS@PLGA NPs were designed using a nano-precipitation-self-assembly method, incorporating the cytotropic sequence iRGD and "eat me" signal molecule phosphatidylserine to specifically target macrophages. The hybrid biomaterial hydrogels were then fabricated by mixing an aqueous solution of gelation and PVA (8wv%) with a Til iRGD&PS@PLGA NPs aqueous solution to obtain Gel@Til iRGD&PS@PLGA NPs (Fig. 6a).

The Til iRGD&PS@PLGA NPs were labeled with Dil fluorescent dye to assess the macrophage targeting efficacy. For comparison, Til-PLGA NPs granules without lipid layer modification were prepared using the same method. Both types displayed similar sizes around 150 nm and showed a single monomodal distribution in particle size (PDI < 0.2), with zeta potentials of -24.6 mV and -28.5 mV, respectively (Fig. 6b, c). *In vitro* release tests showed that Til iRGD&PS@PLGA NPs achieved sustained release of Til over 120 h (Fig. 6d) TEM was employed to confirm the size of Til iRGD&PS@PLGA NPs (Fig. 6e). The fluorescence images showed that Til iRGD&PS@PLGA NPs had an excellent macrophage targeting efficacy (Fig. 6f).

The iRGD&PS@PLGA NPs were water insoluble and displayed no chemical interaction with the hydrogel, as confirmed by the FTIR spectra of the iRGD&PS@PLGA NPs-loaded PVA/gelatin hydrogel sample (Fig. 6e). The FTIR spectra showed a broad band peak at 3283.97 cm^{-1} , which may belong to the O-H stretching of PVA and might be due to inter- and intra- molecular hydrogen bonds. The peak at 1237.61 cm^{-1} may belong to the stretching of the C-N stretching groups of gelation. Besides the abovementioned peaks from the PVA/gelatin hydrogel, distinct peaks from tiliroside were also observed in the FTIR

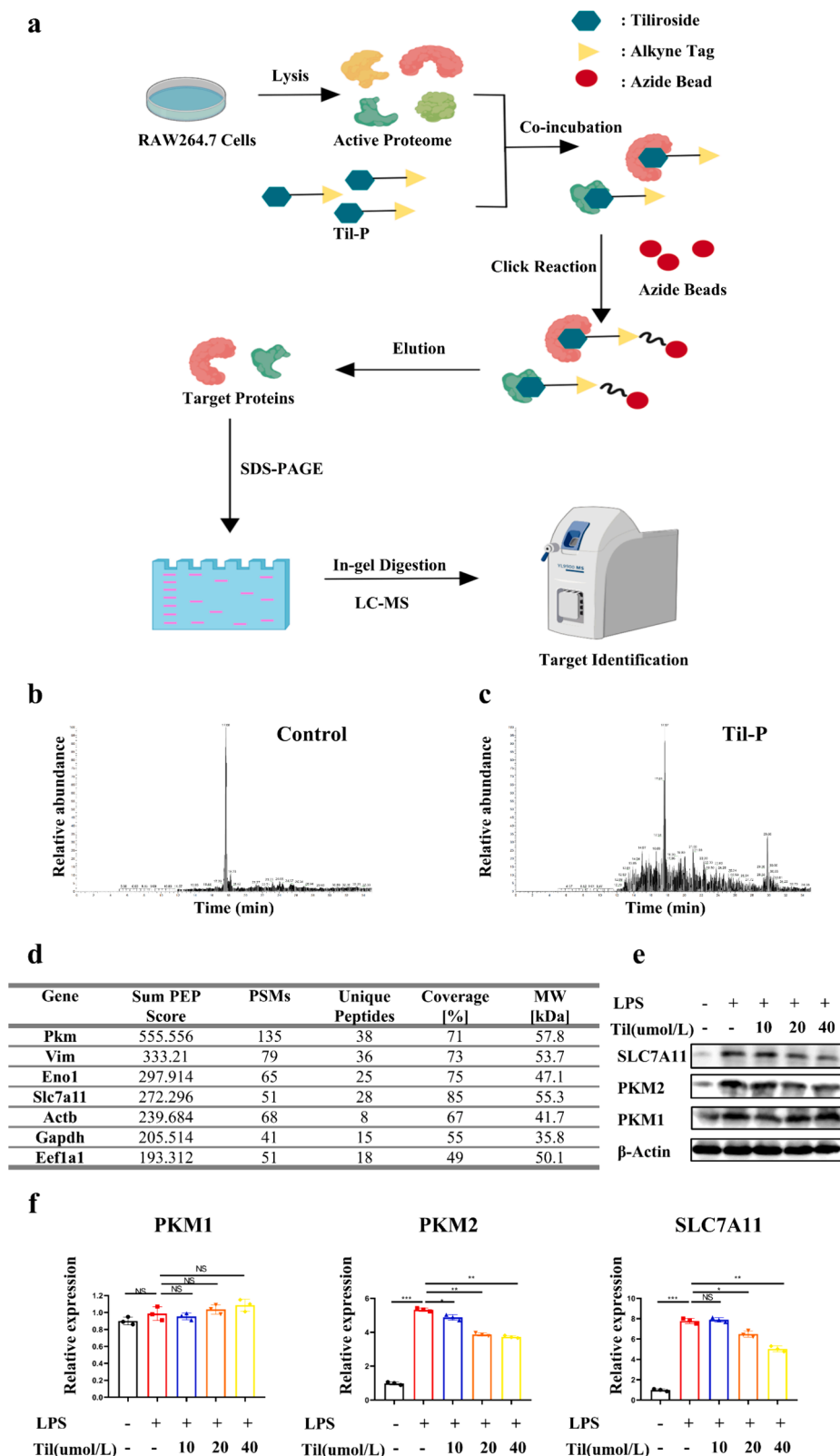


Fig. 2. Potential target proteins of Tilioside were identified by integrating Activity-Based Protein Profiling (ABPP) with Liquid Chromatography–Tandem Mass Spectrometry (LC–MS/MS). (a) The schematic diagram of ABPP experiment. Representative TIC results of control group (b) and Til-P treated group (c) and (d) The table of target proteins identified by LC–MS/MS ranked by the sum of PEP scores. (e) RAW264.7 cells were treated with different concentrations of Til (0, 10, 20, 40 μ M) Til. Representative Western blot of PKM1, PKM2, and SLC7A11 levels in RAW264.7 cells in the presence of LPS (100 ng/mL). (f) Quantitative analysis of PKM1, PKM2, and SLC7A11 protein levels in RAW264.7 cells ($n = 3$). *P value < 0.05; **P value < 0.01; ***P value < 0.001 per; ****P value < 0.0001 per group by unpaired t test.

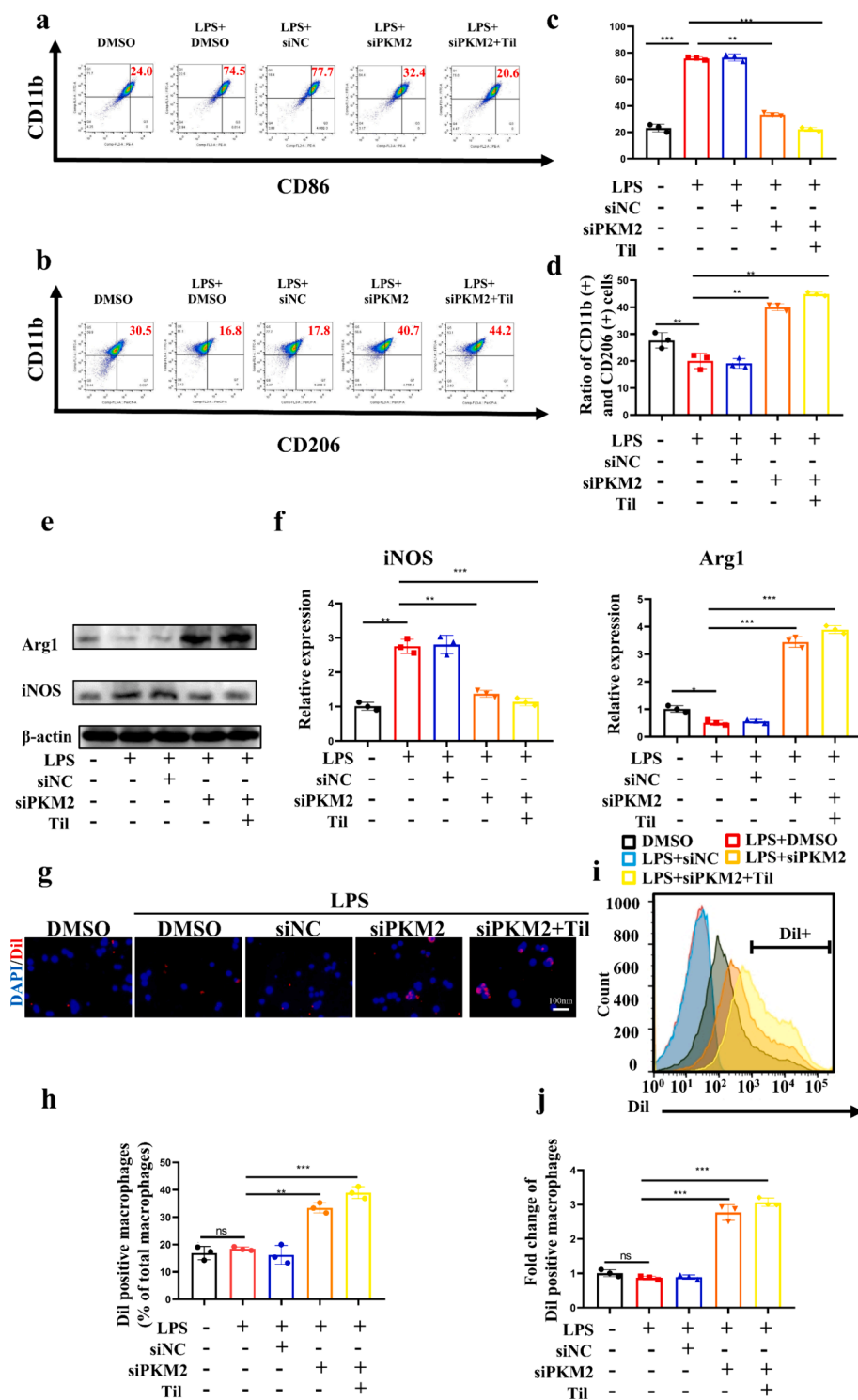


Fig. 3. Til inhibits PKM2 signaling to promote macrophage polarization and efferocytosis. Representative flow cytometry of (a) CD86⁺ cells and (c) CD206⁺ cells. (b) The percentage of M1 phenotypes was quantified as the ratio of CD86⁺ and CD11b⁺ cells (n = 3). (d) The percentage of M2 phenotypes was quantified as the ratio of CD206⁺ and CD11b⁺ cells (n = 3). (e) Representative Western blot of iNOS and Arg1 levels in RAW264.7 cells. (f) Quantitative analysis of iNOS and Arg1 protein levels in RAW264.7 cells (n = 3). (g) ACs and siPKM2-treated BMDMs were incubated with Dil-labeled ACs at time points of 30 min at a AC: BMDMs ratio of 5:1 (n = 3). (h) The percentage of efferocytosis was quantified as the number of BMDMs with engulfed apoptotic cells as a percentage of total BMDMs (n = 3). (i) Representative flow cytometry images for efferocytosis evaluation. (j) Quantification of Dil-positive BMDMs (n = 3). *P value < 0.05; **P value < 0.01; ***P value < 0.001 per; ****P value < 0.0001 per group by unpaired *t* test.

spectra, with the peak at 1743.09 cm⁻¹ indicating C=O the presence of a strong carboxylic group, and the peak at 2815.53 cm⁻¹ corresponding to the C-H bond stretching of the alkyl groups. The hydrogel had a porous structure with pore sizes of ≈100 μm in diameter, with iRGD@PS@PLGA

NPs loading not influencing the pore sizes of the hydrogel (Fig. 6h). The hydrogel films demonstrated a compressive strain between 60 and 80 % (Fig. 6i). Notably, under low pH conditions (pH 5.0), significant pH-induced dissociation of the hydrogel was observed, facilitating fast

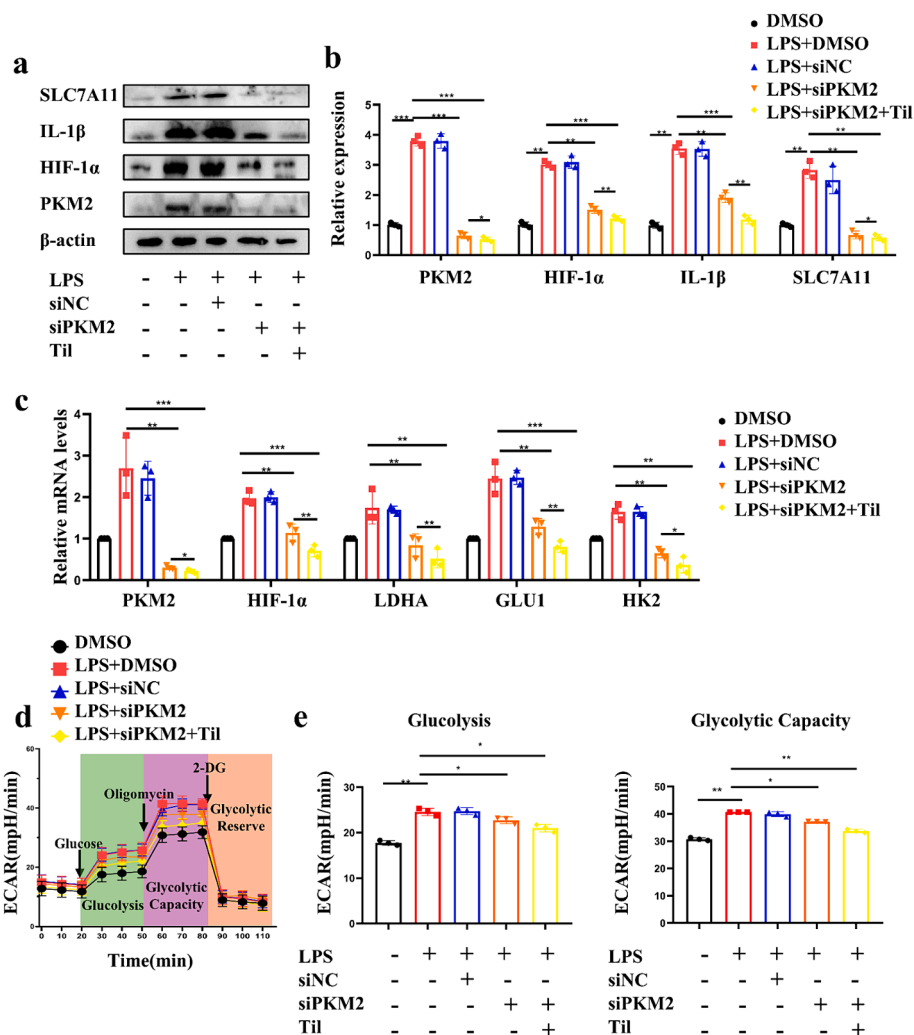


Fig. 4. Til inhibits PKM2 signaling to promote efferocytosis and glycolysis-related macrophage reprogramming. (a) Representative western blot of RAW264.7 cells in different groups in the presence of LPS (100 ng/mL). (b) Quantitative analysis of PKM2, HIF-1 α , IL-1 β and SLC7A11 protein levels in RAW264.7 cells (n = 3). (c) Representative qRT-PCR of macrophages. in different groups in the presence of LPS (100 ng/mL). (d) The ECAR curve shows the glycolysis function of RAW264.7 cells in different groups after pre-incubation for 1 h and stimulation with LPS(100 ng/mL) for 24 h. Vertical lines indicate the time of addition of glucose (10 mmol/L), oligomycin (1 μ mol/L), and 2-DG (50 mmol/L). (e) Glycolysis and glycolytic capacity were determined from ECAR data. *P value < 0.05; **P value < 0.01; ***P value < 0.001 per; ****P value < 0.0001 per group by unpaired *t* test.

release of iRGD&PS@PLGA NPs as well as fast release of Til, thereby catering to the therapeutic efficacy in diabetic wounds (Fig. 6j, k).

3.6. Biocompatibility of Gel@Til iRGD&PS@PLGA NPs

The cell viability on the first, second, and third day did not display significant differences in each group, indicating that Gel@Til iRGD&PS@PLGA NPs exhibited good biocompatibility (Fig. 7a). Then we investigated whether Gel@Til iRGD&PS@PLGA NPs influence macrophages polariton and macrophage-endothelial regulation. As shown in Fig. 7b, macrophages cultured with blank hydrogels Gel@Til-PLGA NPs or Gel@Til iRGD&PS@PLGA NPs in upper co-culture chambers, and MAECs are cultured in the substratum. Flow cytometry results demonstrated that Gel@Til iRGD&PS@PLGA NPs were highly effective in reducing the expression of the proinflammatory biomarker CD86 while increasing the expression of the anti-inflammatory biomarker CD206 in LPS-activated macrophages (Fig. 7c, d, e, f). The scratch, transwell, and tube formation assay were performed to verify whether Gel@Til iRGD&PS@PLGA NPs influence macrophage-endothelial regulation. The results obtained from scratch, transwell, and tube formation assay showed that Gel@Til iRGD&PS@PLGA NPs enhanced the

angiogenesis of mouse aortic endothelial cells (MAECs). (Fig. 7g-l).

To achieve these advantageous effects of tiliroside, we developed a tissue-friendly, pH-responsive hydrogel platform based on the use of gelatin, and PVA. Gelatin and PVA have been incorporated as important components of a pH-sensitive hydrogel due to their unique physico-chemical properties and biodegradability [44]. The release of the drug to be applied from this platform is accelerated under acidic environments. Using macrophage polarization as a target therapeutic point, we further modified this platform as a living material by loading iRGD&PS double-modified lipid nanoparticles. This innovative approach warrants stable incorporation of RGD for cell adhesion and “eat me” signal PS for specific targeting of macrophages. Importantly, Gel@Til iRGD&PS@PLGA NPs significantly promote macrophage efferocytosis and M2 transition as well as improve angiogenesis through macrophage-endothelial regulation *in vitro*.

3.7. Acceleration of diabetic wound healing *in vivo* via Gel@Til iRGD&PS@PLGA NPs

The effect of Gel@Til iRGD&PS@PLGA NPs on wound healing *in vivo* was investigated in HFD/STZ diabetic mice. Full-thickness skin wounds

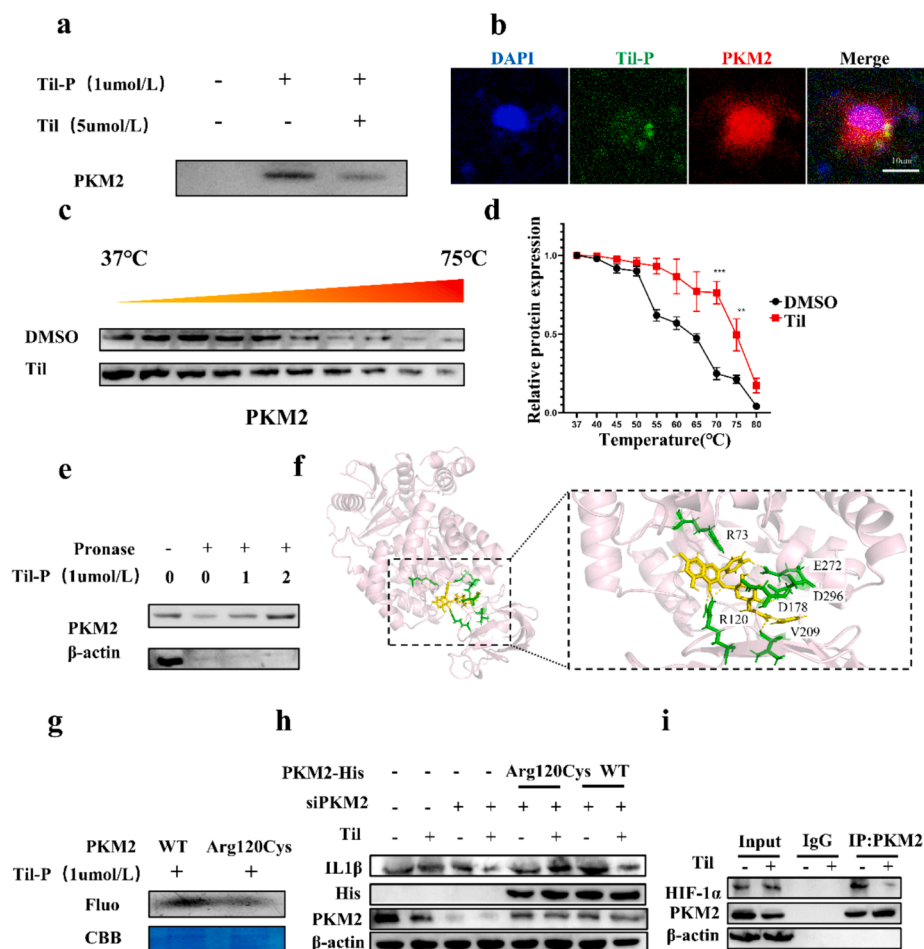


Fig. 5. Til directly binds to PKM2. (a) Verification of Til association with PKM2 through Western blot analysis of pull-down assays conducted in situ. (b) Immunofluorescence labeling demonstrating the colocalization of PKM2 (red) with Til-P conjugated to a FAM dye (green), with a scale bar representing 10 μm. (c, d) Utilization of cellular thermal shift assays for confirming the interaction between Til and PKM2, conducted in triplicate (n = 3). (e, f) Identification of direct binding of Til to PKM2 was determined by DARTS approach. (f) The binding modes and sites of the interaction of Til with PKM2 were predicted using AutoDock Vina software. (g) Fluorescence intensity of recombinant wild-type PKM2 and PKM2-Arg120Cys incubated with Til-P and then click-reacted with a fluorescent dye. (h) PKM2-silenced RAW264.7 cells were transfected with wild-type or mutant PKM2 for 24 h and were then exposed to Til. Protein expression was determined by western blotting. (i) The co-immunoprecipitation assay to evaluate the effect of Til on the levels of the PKM2/HIF1α complex in RAW264.7 cells. *P<0.05, **P<0.01, ***P<0.001 by unpaired *t* test. (For interpretation of the references to colour in this figure legend, the reader is referred to the web version of this article.)

were created on the dorsum of diabetic mice, in which PVA/gelatin hydrogel with PLGA NPs was introduced. The delivery of Til-PLGA NPs with iRGD&PS double modification significantly accelerated wound closure (Fig. 8a, b, and c). Conversely, the delivery of Til without iRGD&PS-modification exhibited less efficacy in promoting skin wound closure than the iRGD&PS-modified group (Fig. 8a, b, and c). To assess the possible impacts on wound healing, skin tissue specimens were examined 14 days post-wounding. Histologically, healed wounds treated with Gel@Til iRGD&PS@PLGA NPs showed a fully regenerated epithelium and a thicker dermis compared to wounds treated with T2DM, blank hydrogels or Gel@Til-PLGA NPs (Fig. 8d). Masson trichrome staining indicated significantly increased collagen deposition in wounds treated with Gel@Til iRGD&PS@PLGA NPs, but not with traditional PVA/gelatin hydrogel delivery system (Fig. 8e), thereby indicating that the enhancement in collagen deposition was dependent response on the delivery of iRGD&PS modified Til-PLGA NPs (Fig. 8e). Collectively, the findings from our study present strong evidence supporting the efficacy of Gel@Til iRGD&PS@PLGA NPs in promoting the repair of skin wounds.

3.8. Acceleration of diabetic wound healing in vivo via Gel@Til iRGD&PS@PLGA NPs through efferocytosis promotion and transitioning Macrophages towards an anti-inflammatory state

Histological analyses of wounded skin tissue showed that F4/80 positive macrophages, located close to and seemingly engulfing LY6G positive neutrophils, were observed in the control group. However, there was a significant reduction in efferocytosis capabilities in the T2DM group. In comparison, wounds treated with Gel@Til iRGD&PS@PLGA NPs exhibited improved efferocytosis compared to those treated with T2DM, blank hydrogels, or Gel@Til-PLGA NPs (Fig. 9a). The intracellular ROS content *in vivo* was analyzed using dihydroethidium (DHE) staining. The application of the Gel@Til-PLGA NPs resulted in a marked reduction in red fluorescence, with the Gel@Til iRGD&PS@PLGA NPs exhibiting the best ROS-scavenging capability, indicating excellent antioxidative effects (Fig. 9b). And LY6G-positive phagocytes and ROS on day 7 in response to various treatments were quantified (Fig. 9c, d). Immunohistochemical staining of wounded skin tissue showed a significant decrease of Arg1 in the T2DM group. Conversely, treatment with Gel@Til iRGD&PS@PLGA NPs can significantly elevate Arg1 level and downregulate the iNOS level, indicating that Gel@Til iRGD&PS@PLGA NPs are capable of regulating

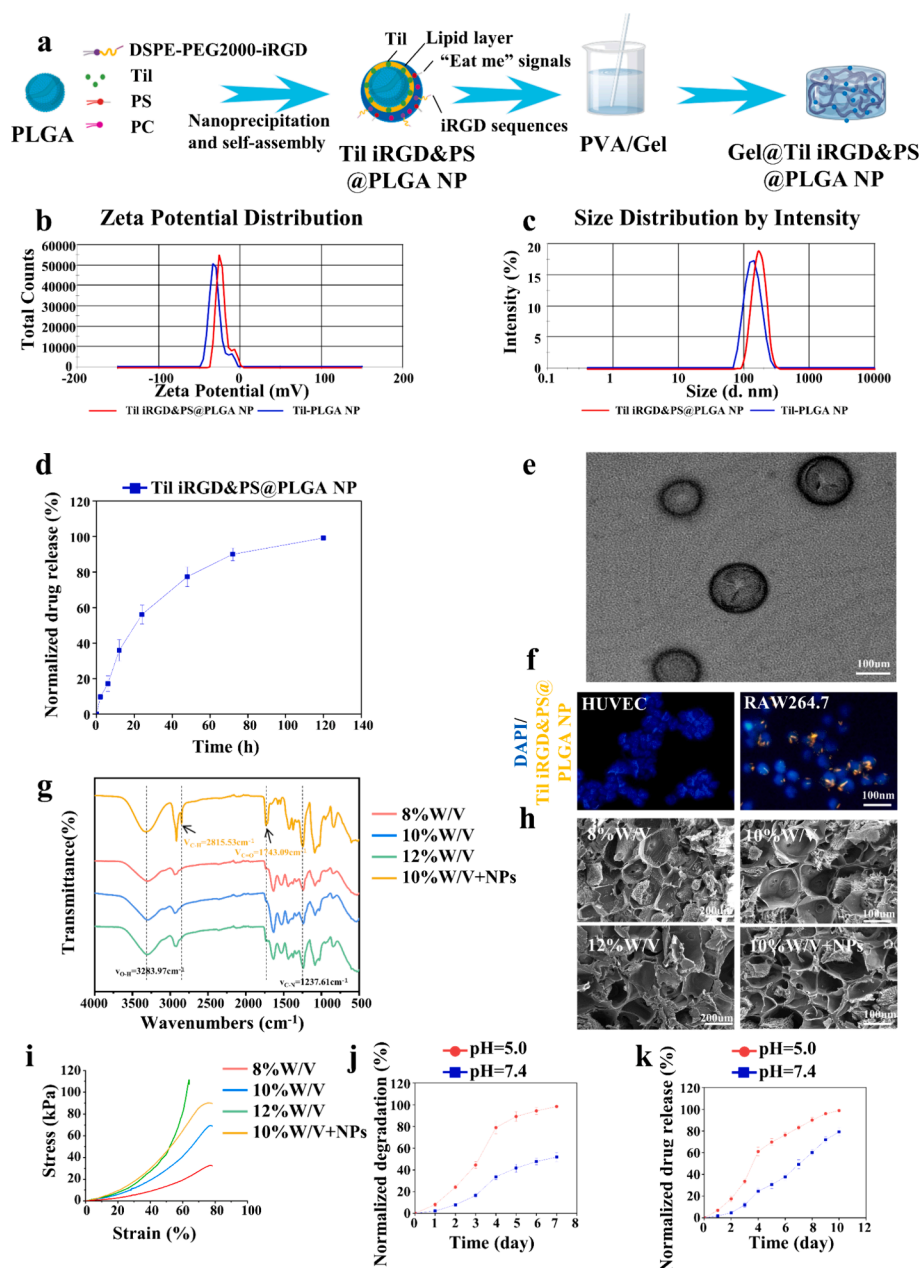


Fig. 6. Characterization of hybrid biomaterial hydrogel. (a) Schematic illustration of the preparation of Gel@Til iRGD&PS@PLGA NPs, (b) zeta potential, (c) Size distribution, (d) The *in vitro* release profile of Til from Til iRGD&PS@PLGA NPs. (e) Til iRGD&PS@PLGA NPs, (f) Fluorescence images of the macrophage targeting character of Til iRGD&PS@PLGA NPs, (g) FT-IR spectra of different hydrogels, (h) TEM images showing the microstructures of different hydrogels, (i) Compressive strain of different hydrogels, (j) The cumulative degradation profiles of hybrid biomaterial hydrogels in PBS with different pH values. (k) The *in vitro* release profile of Til from hybrid biomaterial hydrogels in PBS with different pH values.

the inflammatory microenvironment in diabetic wound sites (Fig. 9e). Besides, Gel@Til iRGD&PS@PLGA NPs can significantly increase the expression of the angiogenesis marker CD31 (Fig. 9f).

In studies utilizing mouse models of diabetic wounds, we have elucidated the therapeutic benefits of Gel@Til iRGD&PS@PLGA NPs in enhancing wound healing, promoting vascular development, facilitating the remodeling and regeneration of granulation tissue, and accelerating re-epithelialization in a live setting. The efficiency of macrophage efferocytosis in wounds treated with Gel@Til iRGD&PS@PLGA NPs showed significant improvement. Histological examinations indicated a reduction in wound-associated inflammation and an enhancement in angiogenesis, extracellular matrix remodeling. A swift decrease in inflammation plays a crucial role in advancing from the inflammatory to the proliferative phase, leading to the remodeling phase in the well-

coordinated wound healing process. The amelioration of oxygen supply in diabetic wounds, attributed to the formation of robust microvessels, likely plays a key role in diminishing inflammation. Furthermore, the use of Gel@Til iRGD&PS@PLGA NPs resulted in the inhibition of HIF-1 α transcriptional activity, thereby decreasing the secretion of pro-inflammatory mediators downstream.

In sum, these results showed that Gel@Til iRGD&PS@PLGA NPs enhance efferocytosis and phenotypic transition of macrophages, downregulate inflammation and oxidative stress, and promote angiogenesis in diabetic wound sites.

4. Conclusion

This study, therefore, effectively demonstrated the feasibility of

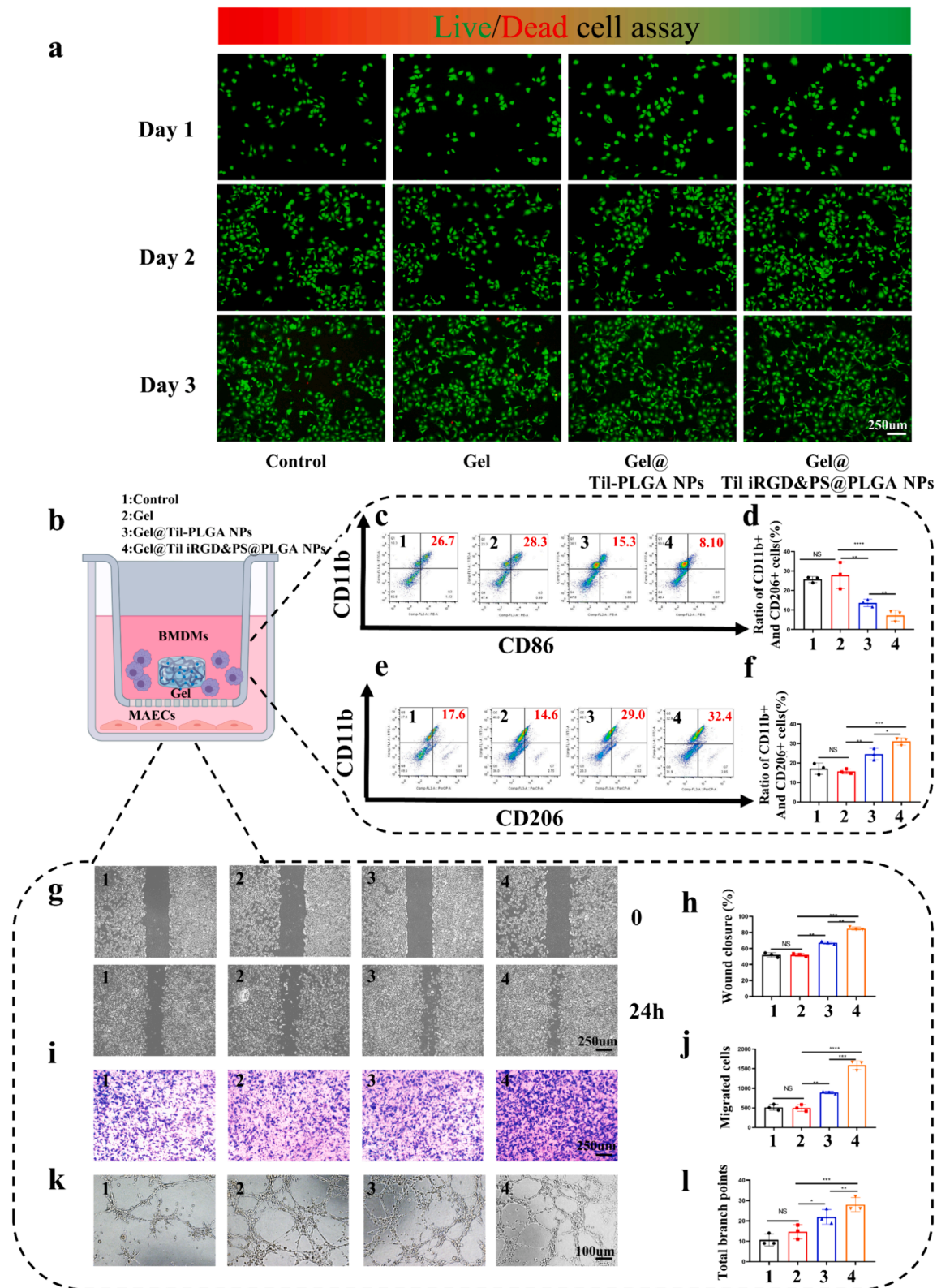


Fig. 7. In vitro evaluation of the anti-inflammatory and angiogenic effects of Gel@Til iRGD&PS@PLGA NPs. (a) Fluorescence images of live/dead staining of HUVECs in different groups. (b) Schematic illustration of the *in vitro* evaluation of Gel@Til iRGD&PS@PLGA NPs. Representative flow cytometry of (c) CD86 + cells and (e) CD206 + cells. (d) The percentage of M1 phenotypes was quantified as the ratio of CD86 + and CD11b + cells (n = 3). (f) The percentage of M2 phenotypes was quantified as the ratio of CD206 + and CD11b + cells (n = 3). (g, h) Wound closure of MAECs of different groups. (i, j) MAECs of different groups were added to the top chamber of a transwell plate and a complete medium containing 10 % FBS was added to the bottom chamber. After 12 h, cells that migrated to the bottom chamber were quantified via image J. (k, l) Endothelial tube formation after co-culturing MAECs together with untreated BMDMs or hydrogel-treated BMDMs. Scale bar: 100 μ m. An Angiogenesis analyzer was used to analyze the branch numbers of MAECs. *P value < 0.05; **P value < 0.01; ***P value < 0.001 per; ****P value < 0.0001 per group by unpaired *t* test.

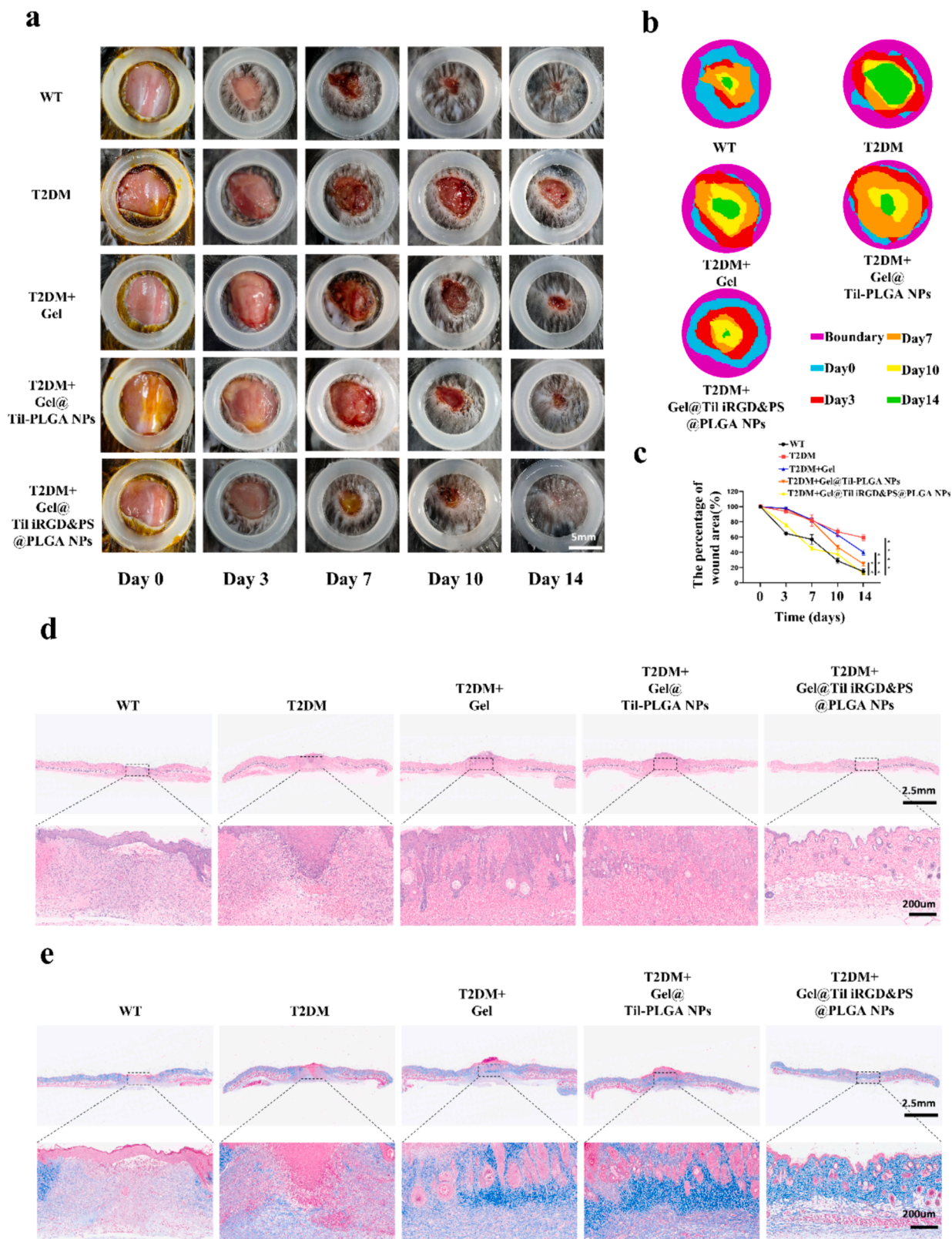


Fig. 8. Gel@Til iRGD&PS@PLGA NPs accelerates DW healing *in vivo*. (a) Photographs of wounds of C57BL/6J mice at different time points after different treatments investigated in this study. (b, c) Quantitative analysis of the relative wound areas at different times (n = 3 biologically independent samples). (d) Representative H&E staining images of wounds on day 14. Scale bar, 2.5 mm (top) and 200 µm (enlarged). (e) Representative Masson Trichrome staining images of wounds on day 14. Scale bar, 2.5 mm (top) and 200 µm (enlarged) (n = 3 biologically independent samples). Data are presented as mean ± SD and statistical significance was analyzed per group by unpaired t test. P value: *P<0.05, **P<0.01, ***P<0.001, **** P<0.0001.

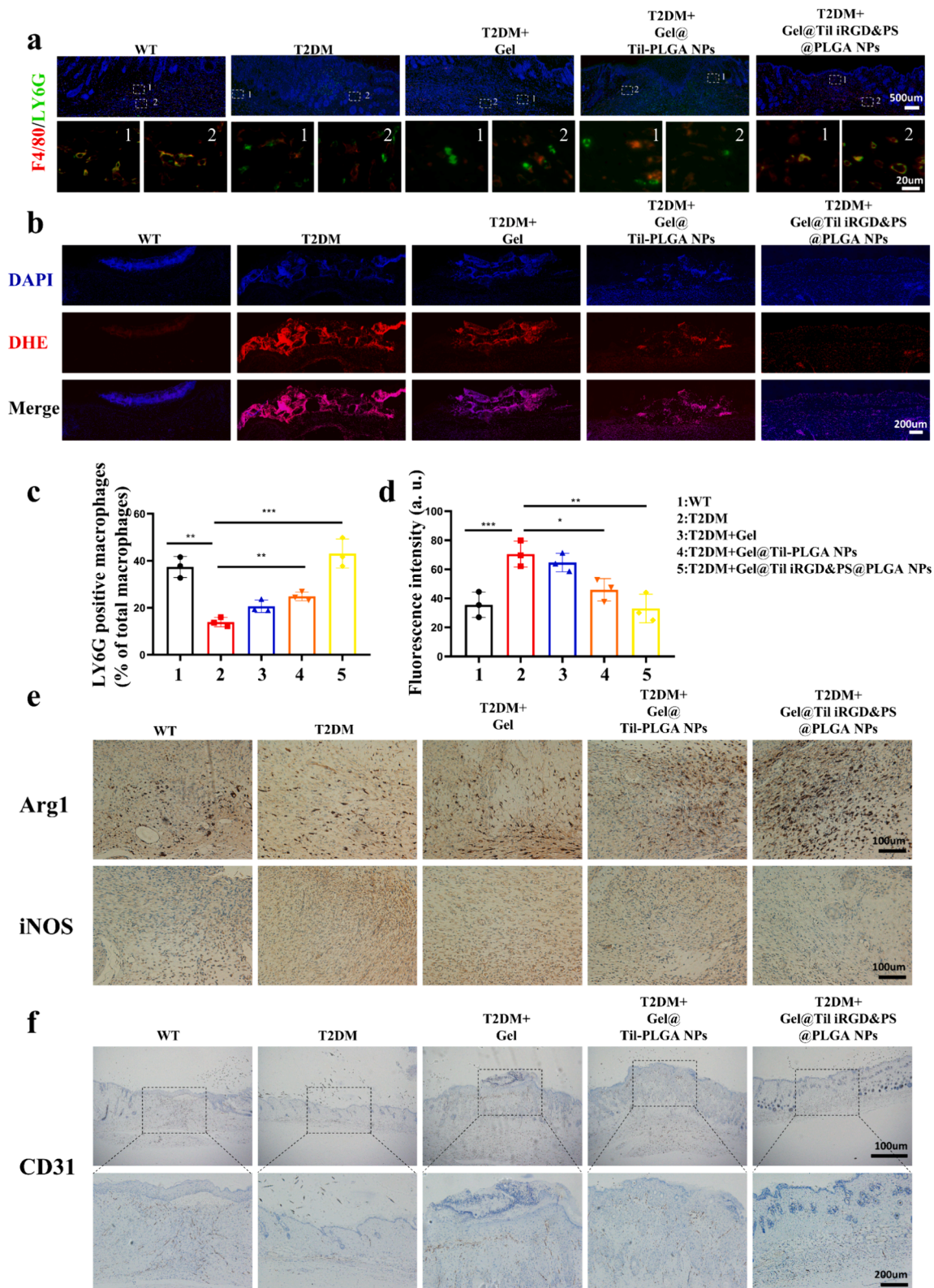


Fig. 9. Gel@Til iRGD&PS@PLGA NPs accelerate DW healing *in vivo* through promoting efferocytosis and glycolysis-related macrophage reprogramming. (a) Localization of F4/80 positive phagocytes in the skin on day 7 after wounding and capturing (LY6G-positive) neutrophils. The designated areas are magnified at the bottom. DAPI staining was employed to mark the nuclei. Measurements are indicated by scale bars: 500 μm for the overall view and 20 μm for detailed observation. (b) Reactive oxygen species (ROS) concentrations within the wound site on the seventh day were quantified using dihydroethidium (DHE) subsequent to various treatments, Scale bar: 200 μm . (c, d) Quantitative investigation of LY6G-positive neutrophils and ROS on day 7 in response to various treatments. The data are presented as the mean \pm s.d. ($n = 3$ independent mice). (e) Immunohistochemical staining was performed at 7 days post-wounded using anti-Arg-1 and anti-iNOS. Scale bar: 100 μm . (f) Immunohistochemical staining was performed at 7 days post-wounded using anti-CD31. Scale bar: 200 μm . Data are presented as mean \pm SD and statistical significance was analyzed via Student's two-sided *t*-test. P value: * $P < 0.05$, ** $P < 0.01$, *** $P < 0.001$, **** $P < 0.0001$.

combining tiliroside with biomaterials as a therapeutic avenue for diabetic wound healing. Our findings suggest that the use of Gel@Til iRGD&PS@PLGA NPs represents a groundbreaking method for enhancing the healing of diabetic wounds. Nevertheless, it is important to note that the diabetic wound models in mice, induced through STZ injection, only mimic a fraction of the intricate pathophysiological processes of diabetic wounds in humans. Consequently, to corroborate the outcomes detailed in this study, further research involving larger mammals or human subjects is essential.

CRedit authorship contribution statement

Wenqian Zhang: Writing – original draft, Methodology, Conceptualization. **Shengming Zhang:** Methodology, Data curation, Conceptualization. **Samuel Knoedler:** Writing – review & editing, Supervision, Methodology. **Wenhao Han:** Writing – review & editing, Supervision, Funding acquisition. **Kangkang Zha:** Methodology. **Hui Li:** Writing – review & editing, Supervision. **Adriana Christine Panayi:** Writing – review & editing, Supervision. **Michael Alftershofer:** Methodology. **Bong-Sung Kim:** Investigation, Funding acquisition. **Weixian Hu:** Methodology, Investigation. **Yanzhi Zhao:** Methodology, Investigation. **Qian Feng:** Supervision, Methodology, Funding acquisition. **Yuval Rinkevich:** Writing – review & editing, Supervision, Investigation, Funding acquisition. **Bobin Mi:** Supervision, Methodology, Funding acquisition. **Guohui Liu:** Writing – review & editing, Supervision, Funding acquisition.

Declaration of competing interest

The authors declare that they have no known competing financial interests or personal relationships that could have appeared to influence the work reported in this paper.

Data availability

No data was used for the research described in the article.

Acknowledgements

This work was supported by the National Science Foundation of China (No. 82272491, No. 82072444); the Wuhan Science and Technology Bureau (2022020801020464); Grants from Hubei Province Unveiling Science and Technology Projects (No.2023AFB1096).

Appendix A. Supplementary data

Supplementary data to this article can be found online at <https://doi.org/10.1016/j.cej.2024.154800>.

References

- [1] S. Vijan Type 2 Diabetes Ann. Intern. Med. 171 9 2019 ITC65-ITC80 10.7326/AITC201911050.
- [2] J.B. Cole, J.C. Florez, Genetics of diabetes mellitus and diabetes complications, Nat. Rev. Nephrol. 16 (7) (2020) 377–390, <https://doi.org/10.1038/s41581-020-0278-5>.
- [3] D.G. Armstrong, T.W. Tan, A.J.M. Boulton, S.A. Bus, Diabetic Foot Ulcers: A Review, J. Am. Med. Assoc. 330 (1) (2023) 62–75, <https://doi.org/10.1001/jama.2023.10578>.
- [4] D.G. Armstrong, A.J.M. Boulton, S.A. Bus, Diabetic Foot Ulcers and Their Recurrence, N. Engl. J. Med. 376 (24) (2017) 2367–2375, <https://doi.org/10.1056/NEJMr1615439>.
- [5] E. Ahmad, S. Lim, R. Lamprey, D.R. Webb, M.J. Davies, Type 2 diabetes, Lancet 400 (10365) (2022) 1803–1820, [https://doi.org/10.1016/S0140-6736\(22\)01655-5](https://doi.org/10.1016/S0140-6736(22)01655-5).
- [6] S.L. Wong, M. Demers, K. Martinod, M. Gallant, Y. Wang, A.B. Goldfine, C.R. Kahn, D.D. Wagner, Diabetes primes neutrophils to undergo NETosis, which impairs wound healing, Nat. Med. 21 (7) (2015) 815–819, <https://doi.org/10.1038/nm.3887>.
- [7] V. Falanga, R.R. Isseroff, A.M. Soulika, M. Romanelli, D. Margolis, S. Kapp, M. Granick, K. Harding, Chronic wounds, Nat. Rev. Dis. Primers 8 (1) (2022) 50, <https://doi.org/10.1038/s41572-022-00377-3>.
- [8] D. Lv, X. Cao, L. Zhong, Y. Dong, Z. Xu, Y. Rong, H. Xu, Z. Wang, H. Yang, R. Yin, M. Chen, C. Ke, Z. Hu, W. Deng, B. Tang, Targeting phenylpyruvate restrains excessive NLRP3 inflammasome activation and pathological inflammation in diabetic wound healing, Cell Rep Med 4 (8) (2023) 101129, <https://doi.org/10.1016/j.xcrmm.2023.101129>.
- [9] M. Rodrigues, N. Kosaric, C.A. Bonham, G.C. Gurtner, Wound Healing: A Cellular Perspective, Physiol. Rev. 99 (1) (2019) 665–706, <https://doi.org/10.1152/physrev.00067.2017>.
- [10] V. Falanga, Wound healing and its impairment in the diabetic foot, Lancet 366 (9498) (2005) 1736–1743, [https://doi.org/10.1016/S0140-6736\(05\)67700-8](https://doi.org/10.1016/S0140-6736(05)67700-8).
- [11] S.A. Eming, P. Martin, M. Tomic-Canic, Wound repair and regeneration: mechanisms, signaling, and translation, Sci. Transl. Med. 6 (265) (2014) 265sr6, <https://doi.org/10.1126/scitranslmed.3009337>.
- [12] R. Medzhitov, Origin and physiological roles of inflammation, Nature 454 (7203) (2008) 428–435, <https://doi.org/10.1038/nature07201>.
- [13] C. Han, Y. Nie, H. Lian, R. Liu, F. He, H. Huang, S. Hu, Acute inflammation stimulates a regenerative response in the neonatal mouse heart, Cell Res. 25 (10) (2015) 1137–1151, <https://doi.org/10.1038/cr.2015.110>.
- [14] O. Soehnlein, L. Lindbom, Phagocyte partnership during the onset and resolution of inflammation, Nat. Rev. Immunol. 10 (6) (2010) 427–439, <https://doi.org/10.1038/nri2779>.
- [15] M. Peiseler, P. Kubers, More friend than foe: the emerging role of neutrophils in tissue repair, J. Clin. Invest. 129 (7) (2019) 2629–2639, <https://doi.org/10.1172/JCI124616>.
- [16] C. Silvestre-Roig, Q. Braster, A. Ortega-Gomez, O. Soehnlein, Neutrophils as regulators of cardiovascular inflammation, Nat. Rev. Cardiol. 17 (6) (2020) 327–340, <https://doi.org/10.1038/s41569-019-0326-7>.
- [17] A. Ortega-Gomez, M. Perretti, O. Soehnlein, Resolution of inflammation: an integrated view, EMBO Mol. Med. 5 (5) (2013) 661–674, <https://doi.org/10.1002/emmm.201202382>.
- [18] P. Mehrotra, K.S. Ravichandran, Drugging the efferocytosis process: concepts and opportunities, Nat. Rev. Drug Discov. 21 (8) (2022) 601–620, <https://doi.org/10.1038/s41573-022-00470-y>.
- [19] T.A. Wynn, K.M. Vannella, Macrophages in Tissue Repair, Regeneration, and Fibrosis, Immunity 44 (3) (2016) 450–462, <https://doi.org/10.1016/j.immuni.2016.02.015>.
- [20] E. Boada-Romero, J. Martinez, B.L. Heckmann, D.R. Green, The clearance of dead cells by efferocytosis, Nat. Rev. Mol. Cell Biol. 21 (7) (2020) 398–414, <https://doi.org/10.1038/s41580-020-0232-1>.
- [21] G.P. Fadini, L. Menegazzo, M. Rigato, V. Scattolini, N. Poncina, A. Bruttocao, S. Ciciliot, F. Mammano, C.D. Ciobotaru, E. Brocco, M.C. Marescotti, R. Cappellari, G. Arrigoni, R. Million, S. Vigili de Kreutzenberg, M. Albiero, A. Avogaro, NETosis Delays Diabetic Wound Healing in Mice and Humans, Diabetes 65 (4) (2016) 1061–1071, <https://doi.org/10.2337/db15-0863>.
- [22] J. Pang, M. Maienschein-Cline, T.J. Koh, Enhanced Proliferation of Ly6C(+) Monocytes/Macrophages Contributes to Chronic Inflammation in Skin Wounds of Diabetic Mice, J. Immunol. 206 (3) (2021) 621–630, <https://doi.org/10.4049/jimmunol.2000935>.
- [23] P. Doddapattar, R. Dev, M. Ghatge, R.B. Patel, M. Jain, N. Dhanesha, S.R. Lentz, A. K. Chauhan, Myeloid Cell PKM2 Deletion Enhances Efferocytosis and Reduces Atherosclerosis, Circ. Res. 130 (9) (2022) 1289–1305, <https://doi.org/10.1161/CIRCRESAHA.121.320704>.
- [24] S. Maschalidi, P. Mehrotra, B.N. Keceli, H.K.L. De Cleene, K. Lecomte, R. Van der Cruyssen, P. Janssen, J. Pinney, G. van Loo, D. Elewaat, A. Massie, E. Hoste, K. S. Ravichandran, Targeting SLC7A11 improves efferocytosis by dendritic cells and wound healing in diabetes, Nature 606 (7915) (2022) 776–784, <https://doi.org/10.1038/s41586-022-04754-6>.
- [25] S. Rui, Y. Ma, W. Deng, SLC7A11: a new regulator in diabetic wound healing, Signal Transduct. Target. Ther. 7 (1) (2022) 320, <https://doi.org/10.1038/s41392-022-01171-z>.
- [26] C. Hu, J.F. Zhao, Y.M. Wang, X.L. Wu, L. Ye, Tiliroside induces ferroptosis to repress the development of triple-negative breast cancer cells, Tissue Cell 83 (2023) 102116, <https://doi.org/10.1016/j.tice.2023.102116>.
- [27] R. Velagapudi, F. Jamshaid, I. Lepiarz, F.O. Katola, K. Hemming, O.A. Olajide, The tiliroside derivative, 3-O-[(E)-(2-oxo-4-(p-tolyl) but-3-en-1-yl)] kaempferol produced inhibition of neuroinflammation and activation of AMPK and Nrf2/HO-1 pathways in BV-2 microglia, Int. Immunopharmacol. 77 (2019) 105951, <https://doi.org/10.1016/j.intimp.2019.105951>.
- [28] T. Goto, A. Teraminami, J.Y. Lee, K. Ohyama, K. Funakoshi, Y.I. Kim, S. Hirai, T. Uemura, R. Yu, N. Takahashi, T. Kawada, Tiliroside, a glycosidic flavonoid, ameliorates obesity-induced metabolic disorders via activation of adiponectin signaling followed by enhancement of fatty acid oxidation in liver and skeletal muscle in obese-diabetic mice, J. Nutr. Biochem. 23 (7) (2012) 768–776, <https://doi.org/10.1016/j.jnutbio.2011.04.001>.
- [29] G. Li, C.N. Ko, D. Li, C. Yang, W. Wang, G.J. Yang, C. Di Primo, V.K.W. Wong, Y. Xiang, L. Lin, D.L. Ma, C.H. Leung, A small molecule HIF-1 α stabilizer that accelerates diabetic wound healing, Nat. Commun. 12 (1) (2021) 3363, <https://doi.org/10.1038/s41467-021-23448-7>.
- [30] W. Qiao, C. Zhao, N. Qin, H.Y. Zhai, H.Q. Duan, Identification of trans-tiliroside as active principle with anti-hyperglycemic, anti-hyperlipidemic and antioxidant effects from *Potentilla chinensis*, J. Ethnopharmacol. 135 (2) (2011) 515–521, <https://doi.org/10.1016/j.jep.2011.03.062>.

- [31] H. Matsuda, K. Ninomiya, H. Shimoda, M. Yoshikawa, Hepatoprotective principles from the flowers of *Tilia argentea* (linden): structure requirements of tiliroside and mechanisms of action, *Bioorg. Med. Chem.* 10 (3) (2002) 707–712, [https://doi.org/10.1016/S0968-0896\(01\)00321-2](https://doi.org/10.1016/S0968-0896(01)00321-2).
- [32] X. Jin, S. Song, J. Wang, Q. Zhang, F. Qiu, F. Zhao, Tiliroside, the major component of *Agrimonia pilosa* Ledeb ethanol extract, inhibits MAPK/JNK/p38-mediated inflammation in lipopolysaccharide-activated RAW 264.7 macrophages, *Exp Ther Med* 12(1) (2016) 499–505. doi: 10.3892/etm.2016.3305.
- [33] R. Velagapudi, M. Aderogba, O.A. Olajide, Tiliroside, a dietary glycosidic flavonoid, inhibits TRAF-6/NF-kappaB/p38-mediated neuroinflammation in activated BV2 microglia, *Biochim. Biophys. Acta* 1840 (12) (2014) 3311–3319, <https://doi.org/10.1016/j.bbagen.2014.08.008>.
- [34] A.M. Sadaghiani, S.H. Verhelst, M. Bogyo, Tagging and detection strategies for activity-based proteomics, *Curr. Opin. Chem. Biol.* 11 (1) (2007) 20–28, <https://doi.org/10.1016/j.cbpa.2006.11.030>.
- [35] J. Xu, X. Li, K. Ding, Z. Li, Applications of Activity-Based Protein Profiling (ABPP) and Bioimaging in Drug Discovery, *Chem. Asian J.* 15 (1) (2020) 34–41, <https://doi.org/10.1002/asia.201901500>.
- [36] E.M. Palsson-McDermott, A.M. Curtis, G. Goel, M.A.R. Lauterbach, F.J. Sheedy, L.E. Gleeson, M.W.M. van den Bosch, S.R. Quinn, R. Domingo-Fernandez, D.G. Johnston, J.K. Jiang, W.J. Israelsen, J. Keane, C. Thomas, C. Clish, M. Vander Heiden, R.J. Xavier, L.A.J., O'Neill, Pyruvate Kinase M2 Regulates Hif-1alpha Activity and IL-1beta Induction and Is a Critical Determinant of the Warburg Effect in LPS-Activated Macrophages, *Cell Metab.* 21 (2) (2015) 347, <https://doi.org/10.1016/j.cmet.2015.01.017>.
- [37] E.M. Palsson-McDermott, A.M. Curtis, G. Goel, M.A. Lauterbach, F.J. Sheedy, L.E. Gleeson, M.W. van den Bosch, S.R. Quinn, R. Domingo-Fernandez, D.G. Johnston, J.K. Jiang, W.J. Israelsen, J. Keane, C. Thomas, C. Clish, M. Vander Heiden, R.J. Xavier, L.A. O'Neill, Pyruvate kinase M2 regulates Hif-1alpha activity and IL-1beta induction and is a critical determinant of the warburg effect in LPS-activated macrophages, *Cell Metab* 21(1) (2015) 65–80. doi: 10.1016/j.cmet.2014.12.005.
- [38] M. Xie, Y. Yu, R. Kang, S. Zhu, L. Yang, L. Zeng, X. Sun, M. Yang, T.R. Billiar, H. Wang, L. Cao, J. Jiang, D. Tang, PKM2-dependent glycolysis promotes NLRP3 and AIM2 inflammasome activation, *Nat. Commun.* 7 (2016) 13280, <https://doi.org/10.1038/ncomms13280>.
- [39] Q. Li, Y. Wen, L. Wang, B. Chen, J. Chen, H. Wang, L. Chen, Hyperglycemia-induced accumulation of advanced glycosylation end products in fibroblast-like synoviocytes promotes knee osteoarthritis, *Exp. Mol. Med.* 53 (11) (2021) 1735–1747, <https://doi.org/10.1038/s12276-021-00697-6>.
- [40] S.E. Corcoran, L.A. O'Neill, HIF1alpha and metabolic reprogramming in inflammation, *J. Clin. Invest.* 126 (10) (2016) 3699–3707, <https://doi.org/10.1172/JCI84431>.
- [41] P. Luo, Q. Zhang, T.Y. Zhong, J.Y. Chen, J.Z. Zhang, Y. Tian, L.H. Zheng, F. Yang, L. Y. Dai, C. Zou, Z.J. Li, J.H. Liu, J.G. Wang, Celastrol mitigates inflammation in sepsis by inhibiting the PKM2-dependent Warburg effect, *Mil. Med. Res.* 9 (1) (2022) 22, <https://doi.org/10.1186/s40779-022-00381-4>.
- [42] X. Wang, R. Li, H. Zhao, Enhancing angiogenesis: Innovative drug delivery systems to facilitate diabetic wound healing, *Biomed. Pharmacother.* 170 (2024) 116035, <https://doi.org/10.1016/j.biopha.2023.116035>.
- [43] P. Carmeliet, Y. Dor, J.M. Herbert, D. Fukumura, K. Brusselmans, M. Dewerchin, M. Neeman, F. Bono, R. Abramovitch, P. Maxwell, C.J. Koch, P. Ratcliffe, L. Moons, R.K. Jain, D. Collen, E. Keshert, Role of HIF-1alpha in hypoxia-mediated apoptosis, cell proliferation and tumour angiogenesis, *Nature* 394 (6692) (1998) 485–490, <https://doi.org/10.1038/28867>.
- [44] M. Akhlag, A.K. Azad, I. Ullah, A. Nawaz, M. Safdar, T. Bhattacharya, A. Uddin, S. A. Abbas, A. Mathews, S.K. Kundu, M.M. Miret, H.C.A. Murthy, H.P. Nagaswarupa, Methotrexate-Loaded Gelatin and Polyvinyl Alcohol (Gel/PVA) Hydrogel as a pH-Sensitive Matrix, *Polymers (basel)* 13 (14) (2021), <https://doi.org/10.3390/polym13142300>.